https://doi.org/10.5194/egusphere-2025-1931
Preprint. Discussion started: 25 June 2025

Drivers and implications of declining fossil fuel CO_2 in Chinese cities revealed by radiocarbon measurements

Pingyang Li[1,2], Boji Lin[1,2,3], Zhineng Cheng[1,2], Jing Li[1,2], Jun Li[1,2], Duohong Chen[4,*], Tao Zhang[4], Run Lin[1,2], Sanyuan Zhu[1,2], Jun Liu[4], Yujun Lin[4], Shizhen Zhao[1,2], Guangcai Zhong[1,2], Zhenchuan Niu[5,6], Ping Ding[7], Gan Zhang[1,2,*]

[1] State Key Laboratory of Advanced Environmental Technology, Guangzhou Institute of Geochemistry, Chinese Academy of Sciences, Guangzhou 510640, People's Republic of China
[2] Guangdong Key Laboratory of Environmental Protection and Resources Utilization, and Joint Laboratory of the Guangdong-Hong Kong-Macao Greater Bay Area for the Environment, Guangzhou Institute of Geochemistry, Chinese Academy of Sciences, Guangzhou 510640, People's Republic of China
[3] University of Chinese Academy of Sciences, Beijing 100049, People's Republic of China
[4] Environmental Key Laboratory of Regional Air Quality Monitoring, Ministry of Ecology and Environment, Guangdong Ecological and Environmental Monitoring Center, Guangzhou 510308, People's Republic of China
[5] State Key Laboratory of Loess, Institute of Earth Environment, Chinese Academy of Sciences, Xi'an 710061, People's Republic of China
[6] Institute of Global Environmental Change, Xi'an Jiaotong University, Xi'an 710061, People's Republic of China
[7] State Key Laboratory of Deep Earth Processes and Resources, Guangzhou Institute of Geochemistry, Chinese Academy of Sciences, Guangzhou 510640, People's Republic of China

Correspondence to: Gan Zhang (zhanggan@gig.ac.cn), Duohong Chen (chenduohong@139.com)

Abstract. China's clean air policies have successfully mitigated fossil fuel CO_2 (CO_{2ff} or C_{ff}) emissions in bottom-up inventories since 2013. Yet, evidence from top-down measurements and their underlying drivers remains lacking. Here, we quantify C_{ff} concentrations and fuel-specific contributions using atmospheric $\Delta(^{14}CO_2)$ and $\delta(^{13}CO_2)$ measurements across representative Chinese cities. We found distinct regional trends: megacities like Guangzhou show significant C_{ff} declines (35 % decrease from 2011 to 2022) along with their source regions, while smaller cities have yet to demonstrate similar reductions. These improvements can be attributed to a 23 % coal consumption reduction, 17 % increased natural gas use (evidenced by stable isotope analysis), and improved combustion efficiency (indicated by 63 % falling $R_{CO/CO2ff}$ ratios). Notably, the three-decade observational record shows steeper declines in urban $R_{CO/CO2ff}$ ratios than inventory estimates, suggesting current emission inventories may underestimate combustion efficiency improvements and CO emission reductions relative to C_{ff} mitigations. These findings indicate nationwide progress toward C_{ff} emission peaks, with megacities leading the transition. They also underscore how coal-to-gas transitions and technological upgrades simultaneously advance air quality and climate goals. Importantly, our results highlight the critical need to integrate top-down observational frameworks (e.g. radiocarbon measurements) with traditional inventories to better capture rapid, policy-driven emission changes and inform future co-benefit optimization strategies.

https://doi.org/10.5194/egusphere-2025-1931
Preprint. Discussion started: 25 June 2025

1 Introduction

As the world's largest energy consumer, China's heavy reliance on fossil fuels has resulted in severe air pollution and substantial fossil fuel CO_2 (CO_{2ff} or C_{ff}) emissions, accounting for 31 % of global fossil CO_2 emissions in 2022 (Friedlingstein et al., 2023b). These emissions pose critical threats to public health and ecological stability. In response, China has enacted progressive policies including the 2013 Clean Air Action Plan (Zheng et al., 2018; Zhang et al., 2019), 2018 Blue Sky Defense Battle, and 2022 Pollution-Carbon Synergy Plan, achieving co-benefits in air quality improvement and C_{ff} mitigation as quantified through bottom-up inventories like Multi-resolution Emission Inventory for China (MEIC) (Shi et al., 2022). However, the effectiveness of these policies in reducing atmospheric C_{ff} concentrations, and the underlying drivers of these reductions, remains unverified and unexplored through top-down observational approaches, creating a critical knowledge gap in climate policy assessment.

Bottom-up inventories and top-down measurements are approaches commonly used to determine atmospheric C_{ff} emissions, but each has inherent limitations that can affect accuracy and reliability. Although bottom-up inventories are available at increasingly higher spatiotemporal resolution (Han et al., 2020), they are time-consuming to compile and update promptly, often lack quantitative estimation of uncertainty (Lo Vullo and Monforti, 2019), and frequently debated in attributing emissions to specific sources (Gurney et al., 2021). In contrast, top-down studies encompass all existing sources within a geographic region but struggle to achieve accurate partitioning of the fossil fuel and biospheric CO_2 contributions. This methodological impasse can be resolved by ^{14}C analysis, which exploits the unique ^{14}C-depletion signature of C_{ff} compared to contemporary biogenic sources (Levin et al., 2003; Turnbull et al., 2006), enabling unambiguous fossil fuel emission quantification.

Urban areas, occupying merely 3 % of global land yet responsible for 75 % of global C_{ff} emissions (reaching 80 % in China) (Dhakal, 2009; Duren and Miller, 2012), represent strategic priorities for emission mitigation. Recent advances in analytical tools can help identify key drivers of urban C_{ff} reductions. $\delta(^{13}CO_2)$ signatures successfully distinguished coal, oil, and natural gas contributions in cities like Beijing and Xi'an (Wang et al., 2022b), while $\Delta CO/C_{ff}$ ratios tracked combustion efficiency variations across national (China, South Korea) and urban (Paris, Heidelberg) scales (Turnbull et al., 2011; Lee et al., 2020; Lopez et al., 2013; Rosendahl, 2022). To address the research gaps mentioned above, we performed spatiotemporal mapping of 2022 C_{ff} concentrations across representative Chinese cities using dual-carbon isotope constraints ($\Delta(^{14}CO_2)$ + $\delta(^{13}CO_2)$) for fuel-specific source attribution. By integrating multi-source inventories with extended $\Delta CO/C_{ff}$ observations through 2022, we developed a robust framework for top-down verification of policy-driven emission reductions. Our methodology not only quantifies C_{ff} concentration decreases but also identifies the key mechanisms behind these reductions, offering critical insights for refining climate mitigation strategies and supporting sustainable urban development.

https://doi.org/10.5194/egusphere-2025-1931
Preprint. Discussion started: 25 June 2025

2 Data and methods

2.1 Sample collection

We selected representative Chinese cities of varied population sizes for this study: Guangzhou, Shenzhen, and Beijing for megacities (urban permanent resident populations >10 million), Xi'an for supercities (5−10 million), Zhanjiang for large cities (1−5 million), and Shaoguan for medium and small cities (<1 million), which is retrieved from the Tabulation on 2020 China Population Census by County (Council, 2022). Since we could obtain results in Beijing and Xi'an from previous studies, we conducted field sampling in the four cities in Guangdong Province, China (Fig. 1). Guangdong Province is located south of the Nanling Mountains and on the coast of the South China Sea, lying within subtropical and tropical low-latitude regions. The area experiences a prevailing southeast monsoon from the ocean during summer and a northeast monsoon from the continent during winter. The four cities in Guangdong Province differ in terms of area, population, gross domestic product (GDP), C_{ff} inventory emissions, population density, topographic elevation, and land use/land cover. Guangzhou and Shenzhen represent two of China's seven megacities — approximately 45 exist globally — within the Pearl River Delta (PRD), the world's largest urban agglomeration. Guangzhou, the capital of Guangdong Province, has a population of 18.7 million, GDP of 2 884 billion Yuan, and built-up area covering 35.2 %. Shenzhen, a high-tech hub transformed by post-1978 reforms, hosts 17.7 million people with GDP reaching 3 239 billion Yuan and 53.8 % built-up coverage. In contrast, Zhanjiang (large city) and Shaoguan (medium and small city) have smaller populations — 7.0 million and 2.9 million respectively — and lower GDPs of 371.3 billion Yuan and 156.4 billion Yuan. Zhanjiang features extensive cultivated land (47.8 %) and coastal ports, while Shaoguan is distinguished by 78.4 % vegetation coverage.

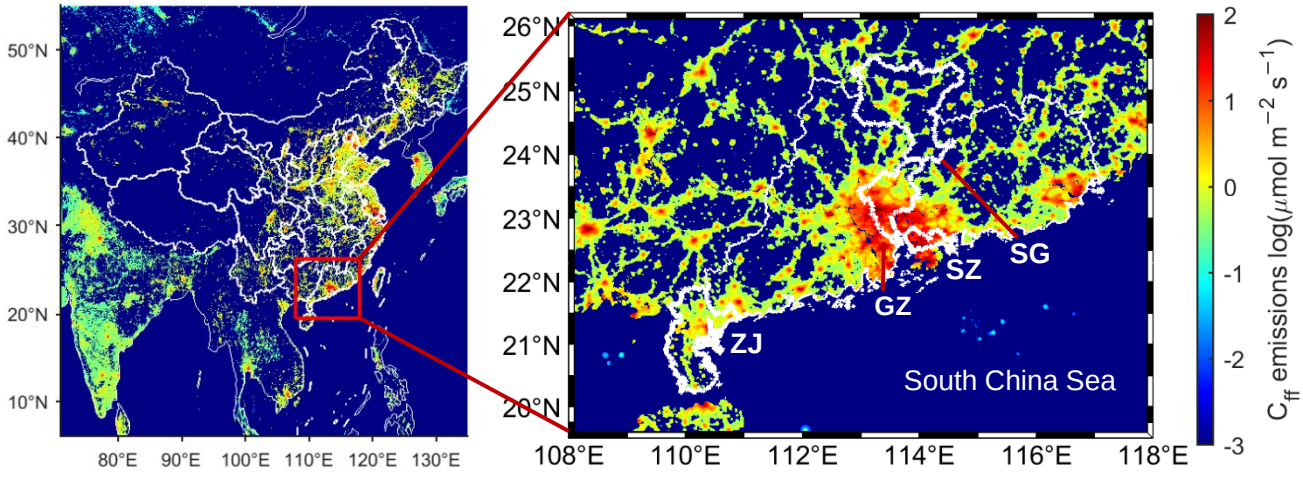

https://doi.org/10.5194/egusphere-2025-1931
Preprint. Discussion started: 25 June 2025

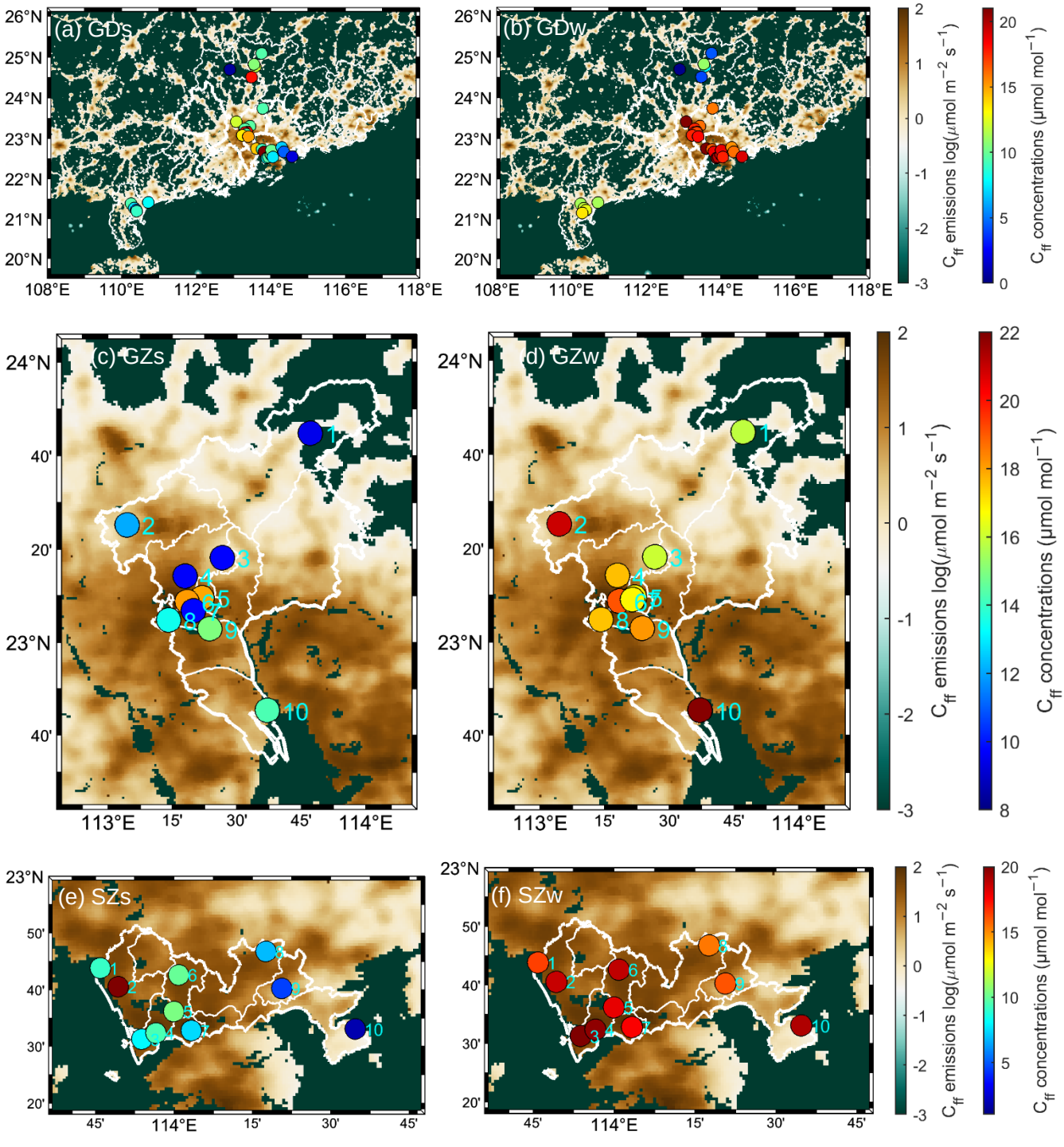

https://doi.org/10.5194/egusphere-2025-1931
Preprint. Discussion started: 25 June 2025

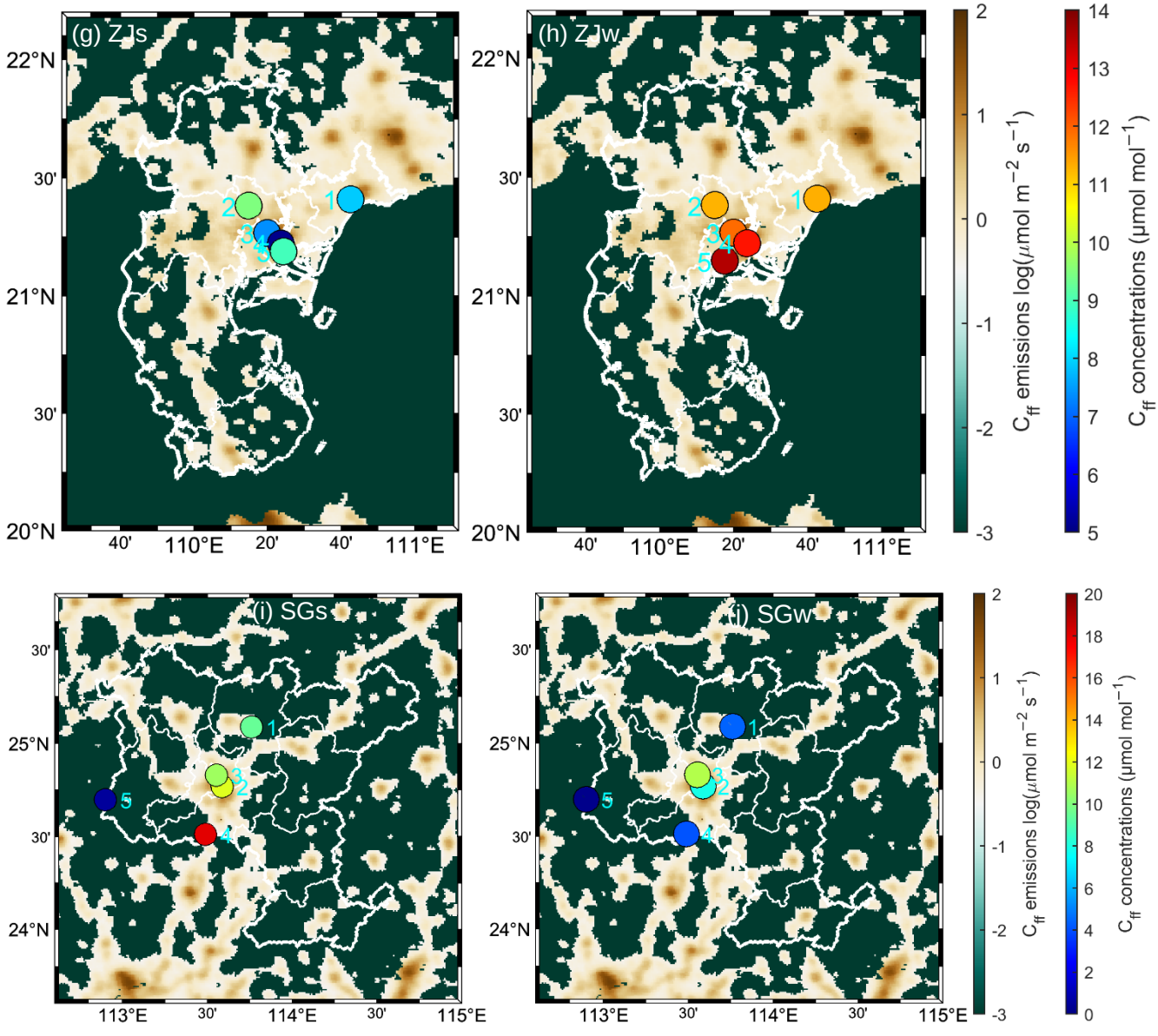

Figure 1: Locations of sampling sites and spatial distribution of C_{ff} concentrations during summer (s) and winter (w) in (a and b, GD) Guangdong Province and the cities of (c and d, GZ) Guangzhou, (e and f, SZ) Shenzhen, (g and h, ZJ) Zhanjiang, and (i and j, SG) Shaoguan. The colored circles represent the observations, while the shading indicates the C_{ff} inventory emissions from the Open-source Data Inventory for Anthropogenic CO_2 (ODIAC) (Oda and Maksyutov, 2024) in August and December with 1×1 km grid spacing. White lines indicate boundaries of cities in Guangdong Province (a and b), and boundaries of districts in the four cities (c–j). In (a) and (b), bold white lines indicate boundaries of nine cities of the Pearl River Delta. The left color bar represents the C_{ff} inventory emissions, while the right color bar represents the C_{ff} observations.

We collected 240 air samples from 30 sites during summer (28 July − 30 August 2022) and winter (12 December 2022 − 6 January 2023) seasons, with weekly sampling in both campaigns. The locations and details of these sampling sites are given

https://doi.org/10.5194/egusphere-2025-1931
Preprint. Discussion started: 25 June 2025

in Fig. 1 and Table A1. Ten sampling sites were located in Guangzhou (GZ1–GZ10), ranging from urban downtown to suburban areas, based on distributed C_{ff} emissions from the Open-source Data Inventory for Anthropogenic CO_2 (ODIAC) (Oda and Maksyutov, 2011; Oda and Maksyutov, 2024). Another 10 sampling sites were distributed uniformly throughout Shenzhen (SZ1–SZ10). In Zhanjiang (ZJ1–ZJ5) and Shaoguan (SG1–SG5), five sampling sites were selected in each city, primarily in urban areas, and distributed according to the first and second most dominant wind directions. These sites are located on the tower or on the roof of the building with 10–12 m extendable masts and are chosen to be free from any modifying effects of surrounding skyscrapers. Most of our sampling sites are generally no more than 300 m from the nearest air quality monitoring station. The sampling height is usually kept above 30 m above the ground level to avoid the influence of local sources. We assume that the measurements at the sampling sites in Guangzhou and Shenzhen are statistically sufficient to assess the whole cities, while those in Zhanjiang and Shaoguan are sufficient to assess the urban areas. Air sampling occurred between 13:00 and 17:00 local time, coinciding with the deepest planetary boundary layer and well-mixed atmospheric conditions. Post-filtration samples were transferred into pre-evacuated/flushed 3 L borosilicate flasks using 12 V micro-diaphragm pumps. These delivered a flow rate of 6 L min^{-1} at 25 °C and 101.3 kPa, with pressurization to 172.4–206.8 kPa. The duration of the sampling was approximately 15–20 min in total.

2.2 Measurement of atmospheric CO_2 and $\delta(^{13}C)$

Whole-air samples were dried using magnesium perchlorate at a constant flow rate of 25 mL min^{-1}, controlled by a mass flow controller. The CO_2 concentrations and $\delta(^{13}C)$ values were then measured using a Picarro G2201-i high-precision carbon isotope analyzer (Picarro, Inc., Santa Clara, CA, USA) with cavity ring-down spectroscopy. Each sample was measured for 10 min, and only data from the final 5 min were used to calculate the average CO_2 concentration and $\delta(^{13}C)$ value. Calibration for the CO_2 concentrations and the $\delta(^{13}C)$ values was performed using the method described by Wen et al. (2013) with three standards: (a) (409.47 ± 0.02) ppm (µmol mol^{-1}; similar hereafter), (−8.717 ± 0.013) ‰; (b) (447.78 ± 0.01) µmol mol^{-1}, (−9.759 ± 0.006) ‰; and (c) (503.65 ± 0.01) µmol mol^{-1}, (−11.456 ± 0.004) ‰, obtained from the Chinese Academy of Meteorological Sciences. The CO_2 concentrations of the standards are traceable to the X2019 standard scale maintained by the Central Calibration Laboratory of the World Meteorological Organization, and the $\delta(^{13}C)$ values are traceable to the stable isotope laboratory of the Institute of Arctic and Alpine Research based on the NBS-19 and NBS-20 standards. The $\delta^{13}C$ values were reported relative to the international Vienna Pee Dee Belemnite standard (Coplen, 1996). The precision was better than 0.2 µmol mol^{-1} for CO_2 concentrations and 0.1 ‰ for $\delta(^{13}C)$ values.

2.3 Measurement of atmospheric $\Delta(^{14}C)$

The residual air samples were transferred into a vacuum system at a flow rate of 300 mL min^{-1}. It was then first passed through a cold trap consisting of dry ice and ethanol slurry to freeze out water, followed by passage through a liquid nitrogen

https://doi.org/10.5194/egusphere-2025-1931
Preprint. Discussion started: 25 June 2025

cold trap (−196 °C) to freeze down the CO_2 (Xu et al., 2007). The extracted and purified CO_2 was converted into graphite using the hydrogen reduction method. The graphite was then pressed into an aluminum holder for ^{14}C measurements using an NEC 0.5MV 1.5SDH-2 accelerator mass spectrometer (AMS, National Electrostatics Corporation, USA) (Zhu et al., 2015). Each measurement wheel typically comprises 13 primary standards (oxalic acid II), 13 secondary standards (IAEA-C7), 13 solid process blanks (*p*-phthalic acid), 6 gas process blanks (^{14}C-free CO_2 in synthetic air from a cylinder), and some authentic air samples. The results are presented as $\Delta(^{14}C)$, which is the per mill (‰) deviation from the absolute radiocarbon reference standard, corrected by fractionation and decay (Stuiver and Polach, 1977). We analyzed 17 pairs of parallel air samples to evaluate the quality control and assurance of the entire sampling and laboratory analysis process, including sampling, extraction, graphitization, and AMS measurement. The AMS measurement uncertainty and the average deviation are (2.1 ± 0.3) ‰ and (0.2 ± 2.9) ‰, respectively (see Fig. A1). We thus specify a one-sigma measurement uncertainty of 2.9 ‰ for $\Delta(^{14}C)$ based on these repeat measurements of air samples.

2.4 C_{ff} concentration estimation (incorporated biomass burning emissions)

Recently added atmospheric CO_2 (CO_{2obs} or C_{obs}) is thought to consist of background CO_2 (CO_{2bg} or C_{bg}) and excess CO_2 (CO_{2xs} or C_{xs}). The C_{xs} mainly includes C_{ff} and biogenic CO_2 (CO_{2bio} or C_{bio}). The corresponding $\Delta(^{14}C)$ values are expressed as Δ_{obs}, Δ_{bg}, Δ_{ff} (−1000 ‰, zero ^{14}C content), and Δ_{bio}, respectively. The mass balance equations for atmospheric CO_2 and $\Delta(^{14}C)$ are expressed as follows (Levin et al., 2003):

$$C_{obs} = C_{bg} + C_{xs} = C_{bg} + C_{ff} + C_{bio} \quad (1)$$

$$C_{obs}\Delta_{obs} = C_{bg}\Delta_{bg} + C_{ff}\Delta_{ff} + C_{bio}\Delta_{bio} \quad (2)$$

$$C_{ff} = \frac{C_{obs}(\Delta_{bg}-\Delta_{obs})}{\Delta_{bg}+1000‰} - \frac{C_{bio}(\Delta_{bg}-\Delta_{bio})}{\Delta_{bg}+1000‰} = \frac{C_{obs}(\Delta_{bg}-\Delta_{obs})}{\Delta_{bg}+1000‰} - \beta \quad (3)$$

The added C_{ff} component is determined using Eq. (3). The CO_2 and $\Delta(^{14}C)$ from other sources, such as air-sea exchange (Graven et al., 2018) and nuclear facilities (see Appendix C1), have been neglected owing to their relatively small amounts. The second term (β) represents a disequilibrium correction for the effect of CO_2 sources from biospheric exchange with distinct $\Delta(^{14}C)$ signatures relative to atmospheric values, primarily attributed to heterotrophic respiration (Rh) and biomass burning (BB). We quantified β using integrated modeling frameworks (see Appendixes B and C). The heterotrophic respiration correction (β_{Rh}) was derived from FLEXPART simulations (Pisso et al., 2019) with CASA-GFED4s data (Randerson et al., 2017; Van Der Werf et al., 2017), yielding values of (−0.06 ± 0.03) µmol mol^{-1} in summer and (−0.11 ± 0.04) µmol mol^{-1} in winter. The biomass burning corrections (β_{BB}) was calculated under two assumptions: (1) $\Delta(^{14}C)$ endmembers assume 100 % perennial biomass, and (2) C_{BB} emissions represent 100 % of C_{bio} in EDGAR2024 (covering open and closed combustion) (Edgar, 2024). β_{BB} showed maximum values of (–0.09 ± 0.08) µmol mol^{-1} during summer and (–0.24 ± 0.12) µmol mol^{-1} during winter. The combined correction ($\beta = \beta_{Rh} + \beta_{BB}$) displayed seasonal patterns: (–0.16 ± 0.09) µmol mol^{-1} in summer and (–0.35 ± 0.15) µmol mol^{-1} in winter, contrasting with (−0.5 ± 0.2) µmol mol^{-1} during

https://doi.org/10.5194/egusphere-2025-1931
Preprint. Discussion started: 25 June 2025

summer and (−0.2 ± 0.1) μmol mol^{-1} during winter reported by Turnbull et al. (2009). Notably, this study is the first to integrate BB emissions into C_{ff} estimation frameworks. BB has a greater impact than Rh on disequilibrium corrections, likely due to inventory and assumption differences. While the total corrections align broadly with literature values, the seasonal trends differed inversely from past studies. We applied literature-based corrections to maintain methodological consistency, and the simulated disequilibrium terms further support our conclusions.

2.5 C_{ff} footprint by FLEXPART model

Surface flux sensitivity of C_{ff} were conducted using the FLEXible PARTicle (FLEXPART) dispersion model (version 10.4) (Pisso et al., 2019). The model produced source–receptor relationships, often referred to as "footprints" for atmospheric surface measurements, which represent the response of the observations at a measuring station to a source emission. The footprints are calculated driven by global meteorological fields from the National Centers for Environmental Prediction's Climate Forecast System (CFSv2) Reanalysis model (Saha et al., 2011). They are computed by releasing 10 000 virtual particles from each receptor at each sampling time and tracking them backward for 30 days over the domain of 0°–60° N, 70° E–150° E, with resolution of 0.1°×0.1°.

2.6 Fuel-specific fractions of C_{ff} by Keeling plot and Bayesian mixing model

The method to determine coal, oil, and natural gas (i.e., fossil fuel type) fractions of C_{ff} is described briefly using a Keeling plot (Miller and Tans, 2003) and the Bayesian mixing model (MixSIAR) (Stock et al., 2018). We calculated the excess $\delta(^{13}C)$ (intercepts δ_{xs}, Eq. (4)) above the background level based on the best-fit lines in the Keeling plot. To determine the $\delta(^{13}C)$ of the fossil fuel source (δ_{ff}, Eq. (5)), we estimated the weighted averages of the fossil fractions F_{ff} using a two end-member mixing analysis on C_{xs}. The $\delta(^{13}C)$ of the biogenic source (δ_{bio}) was set to −26.1 ‰, which is the average $\delta(^{13}C)$ value of the background air plus the −16.8 ‰ discrimination by the terrestrial ecosystem (Bakwin et al., 1998). We then estimated the coal, oil, and natural gas fractions of C_{ff} (F_{coal}, F_{oil}, and F_{ng}, Eqs. (6) and (7)) using a Bayesian tracer mixing model framework implemented as an open-source R package. The model used the δ_{ff} values as mixing data and the end-member $\delta(^{13}C)$ signatures of coal, oil, and natural gas as the source data.

We adopted the end-member $\delta(^{13}C)$ signatures measured in Beijing: δ_{coal} = −24.3 ‰, δ_{oil} = (−28.9 ± 0.5) ‰ and δ_{ng} = (−33.2 ± 0.9) ‰ (Wang et al., 2022a). This selection was based on three considerations: First, coal $\delta(^{13}C)$ signatures exhibit remarkable regional stability in China. Second, oil signatures from the Pearl River Mouth Basin of (−28.1 ± 1.6) ‰ (Cheng et al., 2013) show close agreement with Beijing values of (−28.9 ± 0.5) ‰. Third, measured natural gas signatures like (−33.2 ± 0.9) ‰ in Beijing and (−32.0 ± 0.1) ‰ in Xi'an are significantly enriched compared to literature averages [−39.5 ‰

https://doi.org/10.5194/egusphere-2025-1931
Preprint. Discussion started: 25 June 2025

in Beijing and (−38.9 ± 2.6) ‰ in Pearl River Mouth Basin] (Ping et al., 2018; Quan et al., 2018), as using the lower literature values would lead to underestimation of natural gas contributions.

$$\delta_{obs} = C_{bg}(\delta_{bg} - \delta_{xs}) \times \frac{1}{C_{obs}} + \delta_{xs} \quad (4)$$

$$\delta_{xs} = F_{ff}\delta_{ff} + (1 - F_{ff})\delta_{bio} \quad (5)$$

$$\delta_{ff} = F_{coal}\delta_{coal} + F_{oil}\delta_{oil} + F_{ng}\delta_{ng} \quad (6)$$

$$1 = F_{coal} + F_{oil} + F_{ng} \quad (7)$$

2.7 Correlation of C_{ff} and CO and its emission ratio

We calculated Pearson correlation coefficient (r) between C_{ff} and CO enhancement (ΔCO = CO_{obs} − CO_{bg}), and observational emission ratio of ΔCO to C_{ff} ($R_{CO/CO2ff}$) [ppb ppm^{-1} (nmol µmol^{-1}; similar hereafter)] using linear least squares regression. The $R_{CO/CO2ff}$ ratios were derived from the regression slopes of ΔCO versus C_{ff} concentrations. For comparison, the inventory emission ratio of CO to C_{ff} ($I_{CO/CO2ff}$) [ppb ppm^{-1} (nmol µmol^{-1})] was calculated as (Lee et al., 2020):

$$I_{CO/CO2ff} = E_{CO}/E_{CO2ff} \times M_{CO2}/M_{CO} \quad (8)$$

where E_{CO} and E_{CO2ff} represent the total CO and C_{ff} emissions, respectively, in teragrams per year (Tg a^{-1}) from the bottom-up national and urban inventory; and M_X refers to the molar masses of CO and CO_2 in grams per mole (g mol^{-1}).

3 Results and discussions

3.1 Background selection

We conducted atmospheric observations of CO_2 and its carbon isotope composition ($\Delta(^{14}C)$ and $\delta(^{13}C)$) in Guangzhou, Shenzhen, Zhanjiang, and Shaoguan in Guangdong Province, South China, during the summer and winter of 2022. To attribute CO_2 enhancements (C_{xs}) to a particular region, it is necessary to isolate the component of the observed concentration attributable to fluxes within the region by removing the background (Karion et al., 2021). High-elevation mountains, representing the free troposphere, were considered ideal background locations for use in this study (Turnbull et al., 2009). Specifically, the Nanling site (NL, 1700 m above sea level (a.s.l.)), one of the 30 sampling sites of this study (SG5; Table A1), was selected because it serves as the nearest regional background site for the study areas with relatively complex boundary conditions (for more reasons see Appendix D). The "annual" CO_2 and $\Delta(^{14}C)$ averages at NL station, calculated as averages of summer and winter measurements, were (418.5 ± 7.3) µmol mol^{-1} and (−7.1 ± 3.9) ‰, respectively. These values closely match those observed at Jungfraujoch (JFJ, 3580 m a.s.l.) and appear in the upper-right section of the Keeling plot of $\Delta(^{14}C)$ and CO_2 (i.e., scatter plot between $\Delta(^{14}C)$ and inverse of CO_2 mole fractions) representing background conditions (Pataki et al., 2003). This positioning becomes evident when comparing with Waliguan (WLG, 3890 m a.s.l.) station data (Fig. 2). The advantage of using the Keeling plot method to screen background data is that it simultaneously

https://doi.org/10.5194/egusphere-2025-1931
Preprint. Discussion started: 25 June 2025

accounts for both higher values of $\Delta(^{14}C)$ and lower values of CO_2 (Zhou et al., 2024). The $\Delta(^{14}C)$ averages at NL were the highest among the 30 sampling sites considered in this study, with values of (−3.7 ± 1.3) ‰ in summer and (−10.6 ± 0.8) ‰ in winter (Table A1). We selected a regional (rather than urban) background site in 2022 to capture higher C_{ff} concentrations. This approach establishes a lower baseline for analyzing C_{ff} reduction in subsequent sections.

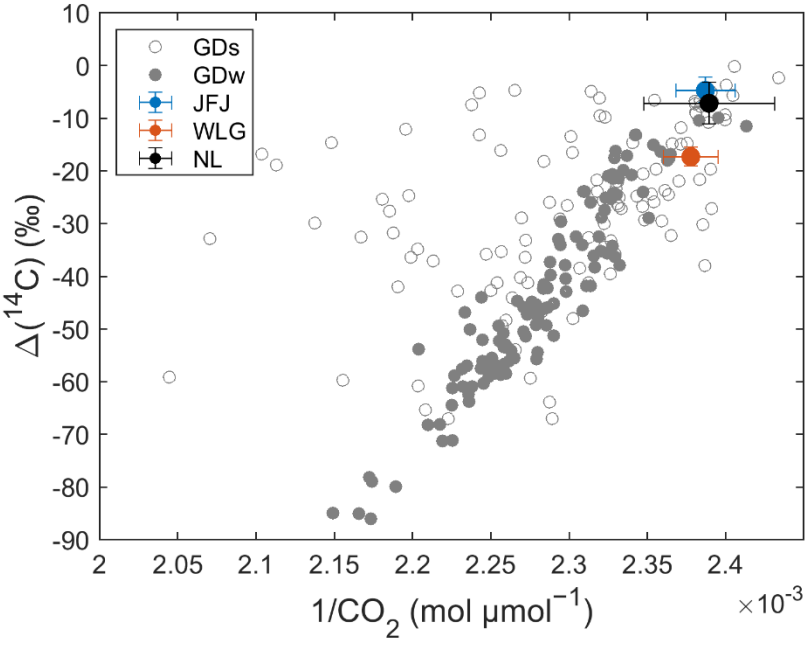

Figure 2: Keeling plot of CO_2 and $\Delta(^{14}C)$ measurements from Guangdong Province in summer (GDs) and winter (GDw), and background stations including JFJ (Jungfraujoch) (Emmenegger et al., 2024b, a), WLG (Waliguan) (Liu et al., 2024; Lan et al., 2023), and NL (Nanling, this study) in 2022. The CO_2 concentrations at the WLG station were obtained from the World Data Centre for Greenhouse Gases (WDCGG, https://gaw.kishou.go.jp/, last accessed: April 21, 2024).

3.2 CO_2, $\Delta(^{14}C)$, C_{xs} and C_{ff} concentrations

CO_2 concentrations in Guangzhou, Shenzhen, Zhanjiang, and Shaoguan were (438.8 ± 12.3), (435.0 ± 12.7), (444.2 ± 17.2), and (431.6 ± 10.5) μmol mol^{-1} (multisite mean and one-sigma standard deviation), respectively; the corresponding $\Delta(^{14}C)$ values were (−40.7 ± 13.4) ‰, (−37.2 ± 24.1) ‰, (−28.8 ± 13.8) ‰, and (−25.0 ± 14.9) ‰, respectively. Relative to the background, CO_2 concentrations in the four cities were enhanced by (20.3 ± 12.5), (16.5 ± 13.5), (25.8 ± 16.7), and (13.1 ± 10.1) μmol mol^{-1} (C_{xs}), respectively; the mean $\Delta(^{14}C)$ was depleted by (−33.6 ± 11.3) ‰, (−29.9 ± 22.3) ‰, (−21.5 ± 11.7) ‰, and (−17.8 ± 15.7) ‰ ($\Delta\Delta(^{14}C)$), respectively, reflecting the marked influence of ^{14}C-free CO_2 emissions from fossil fuel combustion. The fossil fuel and biogenic fractions of C_{xs}, C_{ff} and C_{bio}, were determined using a two end-member mixing analysis. The C_{ff} fractions were (79 ± 5) %, (73 ± 6) %, (59 ± 4) %, and (53 ± 13) % during winter in Guangzhou,

https://doi.org/10.5194/egusphere-2025-1931
Preprint. Discussion started: 25 June 2025

Shenzhen, Zhanjiang, and Shaoguan, respectively. In comparison with other cities worldwide (Table E1, Fig. E1), we observed higher C_{ff} fractions (>70 %) in some megacities and supercities compared with large and medium-sized cities. Noting that the C_{ff}/C_{xs} ratio is critically sensitive to background selection. Regional backgrounds (as implemented here) introduce C_{bio} contributions from surrounding rural/ agricultural sources to C_{xs}, whereas local urban backgrounds effectively isolate urban emissions by filtering out these external biogenic signals, thereby increasing the apparent C_{ff} fraction compared to regional background approaches. The consistent adoption of regional background methodologies across all studies in Table E1 ensures the comparative validity of the results, as they share a common framework for accounting for C_{bio} influences from peripheral non-urban sources. The derived annual C_{ff} averages are (15.3 ± 5.2), (13.7 ± 10.2), (10.0 ± 5.2), and (8.2 ± 7.0) µmol mol^{-1} in Guangzhou, Shenzhen, Zhanjiang, and Shaoguan, respectively, based on the mass balance equations of CO_2 and $\Delta(^{14}C)$. These C_{ff} concentrations were low to moderate compared with those in other cities globally (Table E2, Fig. E1), despite the high emissions in Guangzhou and Shenzhen from inventories (Fig. 1).

3.3 Spatial distribution and seasonal variations

We identified potential source regions of C_{ff} by analyzing its spatial distribution and seasonal variations. C_{ff} is found to be emitted dominantly from densely populated urban downtown areas (GZ6 and GZ5; SG3 and SG2) in Guangzhou during summer (GZs) and Shaoguan during winter (SGw), forming an "urban C_{ff} dome" (Fig. 1cj). This was further supported by significant positive correlations between the C_{ff} measurements and the corresponding gridded ODIAC (Oda and Maksyutov, 2011; Oda and Maksyutov, 2024) inventory emissions in GZs (r = 0.53, p = 0.1) and SGw (r = 0.91, p = 0.03). The "urban C_{ff} dome" indicates that C_{ff} is mainly derived from the localized fossil fuel combustion, which is likely to be influenced by the urban topography. That is, downtown Guangzhou and downtown Shaoguan are surrounded by mountains to the east, north, and west. In contrast, we found that C_{ff} was mainly emitted from western industrial areas (SZ2) in Shenzhen during summer (SZs), and from port areas (ZJ5>ZJ2; ZJ2>ZJ3>ZJ4) in Zhanjiang during winter (ZJw) and summer (ZJs, by atmospheric transport) (Fig. 1ehg).

Atmospheric transmission of C_{ff} from potential source regions was observed at large spatial scales combined with air mass back trajectories by the Hybrid Single-Particle Lagrangian Integrated Trajectory (HYSPLIT) model (Stein et al., 2015) and emission footprints by the FLEXPART dispersion model (Pisso et al., 2019). Shaoguan exhibited higher C_{ff} concentrations in summer ((10.7 ± 8.3) µmol mol^{-1}) than in winter ((5.8 ± 4.4) µmol mol^{-1}). This was likely attributable to atmospheric trapping of emissions from the Pearl River Delta (PRD) urban agglomeration, as illustrated by air mass back trajectories (HYSPLIT, Fig. F1a) and emission footprints (FLEXPART, Fig. 3g), rather than high local emissions due to lower summer emissions from inventories. In contrast, we found higher C_{ff} concentrations in winter compared with those in summer in Guangzhou ((17.7 ± 3.5) > (12.9 ± 5.6) µmol mol^{-1}), Shenzhen ((18.0 ± 9.9) > (9.2 ± 8.5) µmol mol^{-1}), and Zhanjiang ((12.1 ± 5.1) > (7.6 ± 4.3) µmol mol^{-1}), consistent with the values in 14 other Chinese cities (Zhou et al., 2020). The higher winter concentrations found in Guangzhou, Shenzhen, and Zhanjiang in this study likely resulted from atmospheric trapping of

https://doi.org/10.5194/egusphere-2025-1931
Preprint. Discussion started: 25 June 2025

emissions in the shallow planetary boundary layer, and high local emissions, because ODIAC (MEIC) indicates that winter emissions were 8 %, 10 %, and 11 % (17 %, 22 %, and 14 %) higher, respectively, than those in summer (Oda and Maksyutov, 2024; Meic, 2023). The atmospheric trapping of emissions is higher than local emissions during winter in Guangzhou (GZw) and Shenzhen (SZw), which is supported by higher C_{ff} concentrations occurring in downwind areas (GZ2, GZ6, and GZ10; SZ3 and SZ4) compared with upwind areas (GZ1 and GZ3; SZ8 and SZ9). The air mass back trajectories (HYSPLIT, Fig. F1b) and emission footprints (FLEXPART, Fig. 3bd) showed that the major source region was traced to the Yangtze River Delta (YRD) urban agglomeration in East China, and a portion from North China via long-range transport (Fig. F2ef). The major source region from the YRD was also reported in a study of CFC-11 in Shenzhen (Chen et al., 2024).

https://doi.org/10.5194/egusphere-2025-1931
Preprint. Discussion started: 25 June 2025

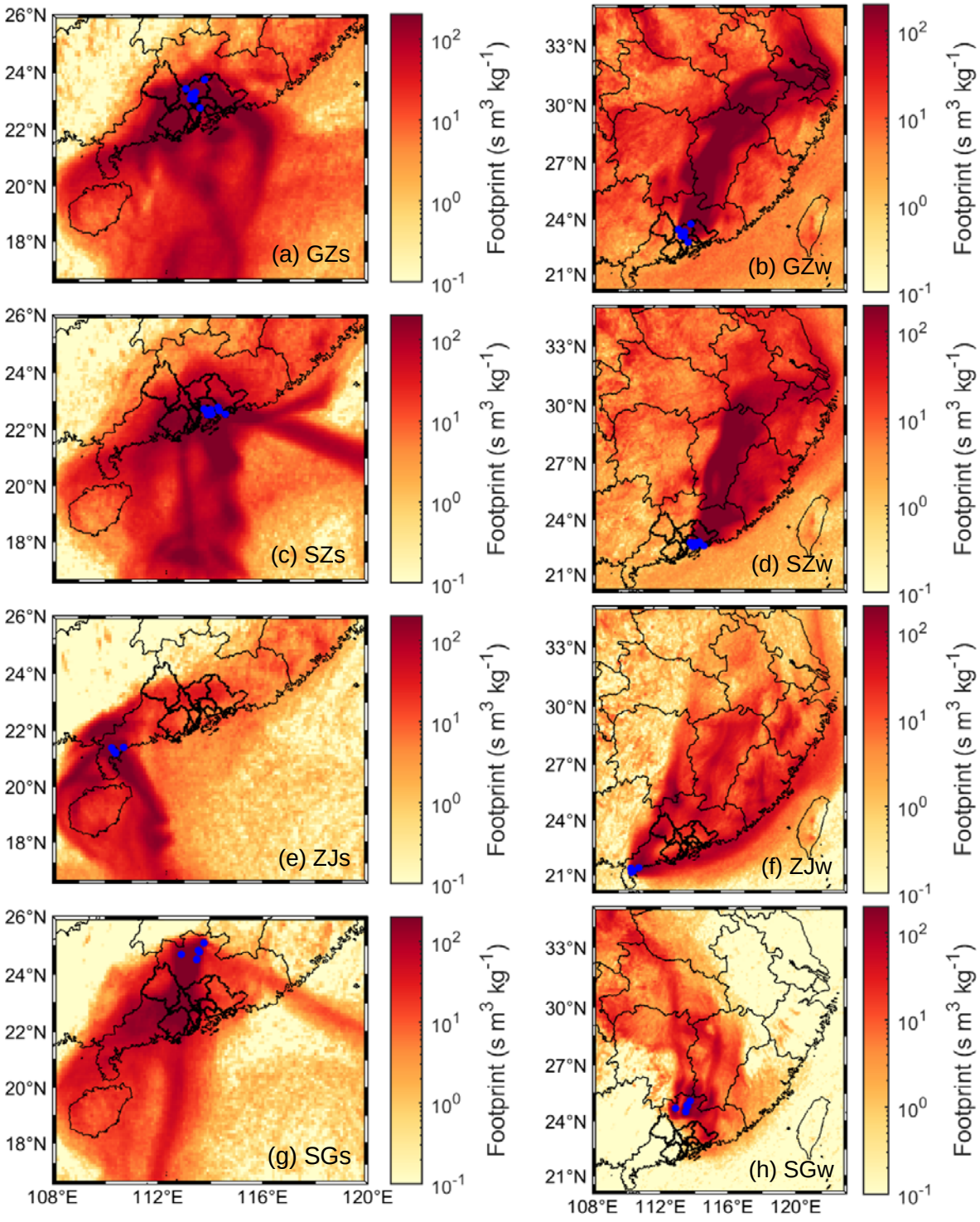

285 **Figure 3: FLEXPART footprints simulating C_{ff} emissions in summer (s) and winter (w) for (a and b, GZ) Guangzhou, (c and d, SZ) Shenzhen, (e and f, ZJ) Zhanjiang, and (g and h, SG) Shaoguan at heights from 0–100 m a.s.l. over a period of 30 days. Blue**

https://doi.org/10.5194/egusphere-2025-1931
Preprint. Discussion started: 25 June 2025

squares are shown as enlarged maps in the right figures. Blue points represent the locations of sampling sites. Black lines indicate the boundaries of continents (left), Chinese provinces (left, bold), and the nine cities of the PRD (right, bold) taken from Natural Earth (https://www.naturalearthdata.com/, last accessed: 9 March 2024).

3.4 Historical variations

We observed a 35 % decline in C_{ff} concentrations in Guangzhou from (23.7 ± 12.9) μmol mol^{-1} in 2010–2011 (Ding et al., 2013) to (15.3 ± 5.2) μmol mol^{-1} in 2022 in this study ($p < 0.01$, two-tailed t-test) (Fig. 4a, Table E2). To conservatively validate this reduction, we employed a dual-method analytical framework for 2022 data designed to maximize C_{ff} estimates: (1) adopting a regional (instead of urban) background to establish a lower baseline, and (2) applying both literature-derived and simulation-based disequilibrium corrections (β) to address potential biases. This validation confirmed 2022 C_{ff} values remain statistical significantly lower than 2010–2011 levels across all the observational data ($p < 0.01$). Additional site-specific validation at GZ7 station showed a 41 % winter reduction from (28.4 ± 15.0) μmol mol^{-1} in 2010 to (16.8 ± 3.4) μmol mol^{-1} in 2022, with equivalent statistical significance ($p < 0.01$). By adjusting baseline assumptions and correction parameters, this methodology ensures that the reported decline is robust against potential overestimations in 2022. It provides reliable evidence for Guangzhou's decarbonization progress, even under maximized C_{ff} calculation scenarios in 2022.

We found that reductions in C_{ff} concentration also occurred in other Chinese cities, and some cities outside China. Statistically significant reductions were observed in Chinese megacities and supercities (Fig. 4a, Table E2): Beijing showed a 32 % decrease from (39.7 ± 36.1) μmol mol^{-1} in 2014 to (27.0 ± 0.3) μmol mol^{-1} in 2014–2016 ($p < 0.05$, two-tailed t-test) and a 50 % decrease to (19.7 ± 22.0) μmol mol^{-1} by winter 2020 ($p < 0.01$); Xi'an decreased by 36 % from (40.1 ± 3.8) μmol mol^{-1} in 2011–2013 to (25.7 ± 1.1) μmol mol^{-1} in 2014–2016 ($p < 0.001$), with suburban areas declining by 12 % from (23.5 ± 6.5) μmol mol^{-1} in 2016 to (13.1 ± 10.9) μmol mol^{-1} in 2021 ($p < 0.05$). These trends are consistent with tree-ring $\Delta(^{14}C)$ records showing peaks in urban C_{ff} emissions for Beijing (2010) and Xi'an (2013) (Niu et al., 2024). Globally, Krakow, Poland showed a 93 % decrease from 27.5 μmol mol^{-1} in 1989 to 1.98–2.18 μmol mol^{-1} in 2005–2009 ($p < 0.001$), Heidelberg, Germany a 2 % decrease from (11.09 ± 0.24) μmol mol^{-1} in 1986–1996 to (10.92 ± 0.34) μmol mol^{-1} in 1997–2007 ($p = 0.04$), and Los Angeles, USA a 42 % decrease from (22.9 ± 5.6) μmol mol^{-1} in 2006–2013 to (13.2 ± 9.4) μmol mol^{-1} in 2014–2016 ($p < 0.01$) (Table E2, Fig. E1). The consistent statistical significance ($p < 0.05$ threshold unless noted) across atmospheric measurements and proxy records underscores the effectiveness of emission mitigation policies in these cities.

We found that C_{ff} concentration reduction did not only occur in the above-mentioned cities, but also probably in their source regions. The winter C_{ff} emission source regions of Guangzhou and Shenzhen are highly overlapped with China's high C_{ff} emitting areas: North China, the YRD in East China, and the PRD in South China (Figs. 3 and F2). These areas are also mostly consistent with the provinces that attained the higher C_{ff} emission reductions due to stricter pollution control policies.

https://doi.org/10.5194/egusphere-2025-1931
Preprint. Discussion started: 25 June 2025

These provinces include Hebei, Shandong, Zhejiang, Shanxi, and Henan in North and East China according to the MEIC inventory (Shi et al., 2022). Therefore, it's very likely that C_{ff} emissions are also decreasing or in a declining growth rate in China's high C_{ff} emitting areas.

Similar reductions were found in C_{ff} emissions from 2012 to 2020 according to the MEIC inventory (Shi et al., 2022), such as Guangzhou (by 16 % from 2011), Shenzhen (by 3 %), Zhanjiang (by 0.1 %), Beijing (by 16 %), and Xi'an (by 9 %) (Fig. 4b), particularly in the industrial and power sectors (Li et al., 2017). We also found such declines in the MIXv2 Asian emission inventory (MIXv2, excluding Shenzhen and Shaoguan) (Li et al., 2024) and another carbon inventory for most Chinese cities (Zhang et al., 2024), but not in the ODIAC (Oda and Maksyutov, 2024) and the Emissions Database for Global Atmospheric Research (EDGAR) (Crippa et al., 2023). In fact, the mitigation of C_{ff} emissions in China's MEIC inventory was primarily driven by heterogeneous trends across cities: 38 % exhibited sustained emission reductions, 29 % showed an initial decline followed by a rebound, while 33 % maintained increasing trajectories. Notably, cities achieving sustained reductions were disproportionately concentrated in larger cities, comprising 86 % of megacities, 43 % of supercities, and 43 % of Type I large cities (populations of 3–5 million). In contrast, smaller cities showed lower mitigation prevalence, with only 34 % of Type II large cities (1–3 million) and 38 % of medium/ small cities attaining emission decreases.

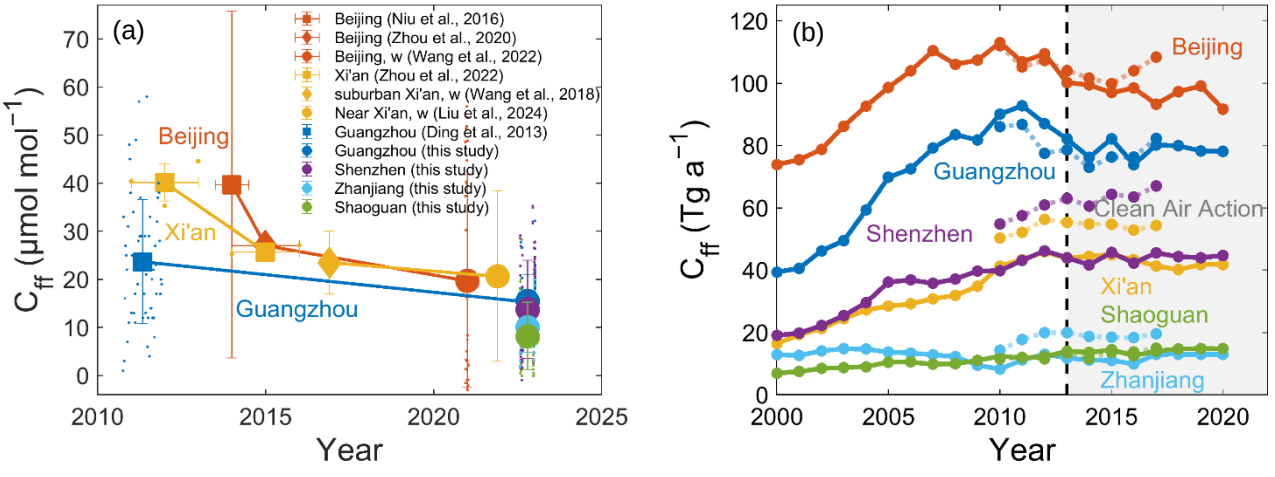

Figure 4: (a) C_{ff} concentrations from atmospheric measurements (Niu et al., 2016; Wang et al., 2022b; Zhou et al., 2022; Ding et al., 2013; Zhou et al., 2020; Wang et al., 2018) in Beijing, Xi'an, Guangzhou, Shenzhen, Zhanjiang, and Shaoguan. The large symbols indicate annual means, multiyear averages, or winter means (w), and the small symbols represent the corresponding scattered measurements. C_{ff} observations are calculated as enhancements over background Nanling for Guangzhou and Waliguan for Beijing and Xi'an. The C_{ff} concentrations in winter in Beijing obtained from Wang et al.[40] were estimated based on the background $\Delta(^{14}CO_2)$ measurements from Waliguan (Liu et al., 2024). The y-axis error bars indicate uncertainty, and the x-axis error bars represent the observed period. (b) C_{ff} emissions from the MEIC (solid lines) (Li et al., 2017; Meic, 2023; Zheng et al., 2018) and MIXv2 (dotted lines) (Li et al., 2024) inventories in Beijing, Xi'an, Guangzhou, Shenzhen, Zhanjiang, and Shaoguan since 2010. The vertical dashed line indicates the year 2013 when China's Clean Air Action Plan was implemented.

https://doi.org/10.5194/egusphere-2025-1931
Preprint. Discussion started: 25 June 2025

3.5 Driver factors

3.5.1 Coal-to-gas transition

We first determined the coal, oil, and natural gas fractions of C_{ff} using the Keeling plot of $\delta(^{13}C)$ and CO_2 (i.e., scatter plot between $\delta(^{13}C)$ and inverse of CO_2 mole fractions) and the Bayesian mixing model (MixSIAR) (Stock et al., 2018) during winter 2022. The fractions in winter were (49 ± 25) %, (29 ± 22) %, and (22 ± 19) %, respectively, for Guangzhou, (47 ± 25) %, (29 ± 21) %, and (24 ± 20) % for Shenzhen, (43 ± 24) %, (29 ± 21) %, and (28 ± 21) % for Zhanjiang, and (39 ± 24) %, (34 ± 23) %, and (27 ± 21) % for Shaoguan. Coal combustion was the largest contributor to C_{ff} emissions, followed in descending order by oil combustion and natural gas combustion. Compared with other cities around the world (Table G1), we found natural gas was the primary fuel type consumed in Paris (70 %) (Lopez et al., 2013) and Beijing [(55 ± 9) %) (Wang et al., 2022b), whereas oil was the main fuel type consumed in Los Angeles (>50 %) (Djuricin et al., 2010; Newman et al., 2016). Coal remains the primary fossil fuel used in Xi'an [(72.6 ± 10.4) % in 2014 and (54 ± 4) % in 2019) (Wang et al., 2022b; Zhou et al., 2014), Guangzhou (49 % in 2022), and Shenzhen (47 % in 2022). Notably, cities with high C_{ff} emissions consume all three types of fossil fuels, with the dominant fuel type varying by city. Coal remains the primary fossil fuel used in many Chinese cities.

The reduction in C_{ff} concentrations can be attributed to changes in energy systems as a result of China's clean air measures (Shi et al., 2022). A major contribution has been the reduction in coal usage and the shift to low-carbon energy sources such as natural gas. During 2013–2022, the share of coal in the energy mix decreased by 4.9 % in China and by 7.1 % in Guangdong Province, whereas the share of natural gas increased by 3.0 % in China and by 7.2 % in Guangdong Province, according to the MEIC inventory (Li et al., 2017; Zheng et al., 2018; Meic, 2023; Xu et al., 2024). By applying the coal, oil, and natural gas fractions of C_{ff} derived from our measurements, it's likely that coal usage in Guangdong Province since 2013 have decreased ≥21 %, and natural gas usage have increased by ≥16 % (Fig. 5a). Similarly, in Guangzhou city, it's likely that coal usage since 2011 has decreased by 23 % instead of by 8.8 % (Fig. 5b), and natural gas usage has increased by 17 % instead of by 7.9 %, assuming that the fuel type fractions of C_{ff} in Guangzhou city were the same as those in Guangdong Province in the inventory.

https://doi.org/10.5194/egusphere-2025-1931
Preprint. Discussion started: 25 June 2025

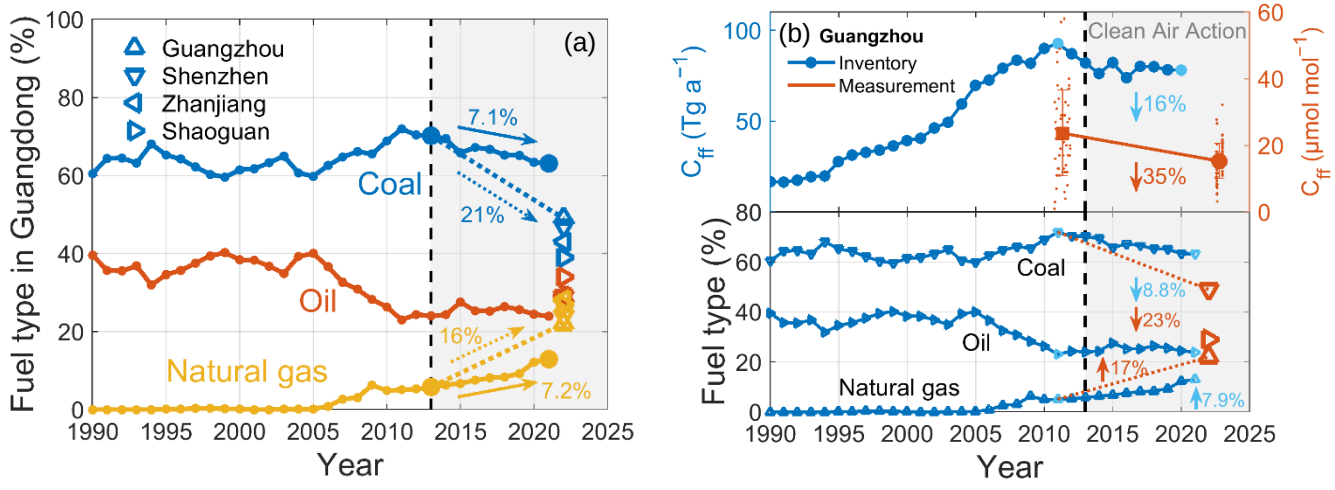

Figure 5: (a) Coal, oil, and natural gas fractions of C_{ff} in Guangdong Province from the MEIC inventory from 1990 to 2021 (points), and in the cities of Guangzhou, Shenzhen, Zhanjiang, and Shaoguan from measurements in this study in 2022 (triangles). (b) (Top) Comparison of reductions in C_{ff} inventory emissions (blue) and measured C_{ff} concentrations (red) resulting from (Bottom) reduced coal usage and increased natural gas usage in Guangzhou. The vertical dashed line indicates the year 2013 when China's Clean Air Action Plan was implemented.

3.5.2 Combustion efficiency improvement

We first calculated $R_{CO/CO2ff}$ ratios at each measurement site and found higher ratios in summer than winter (Fig. H1). However, we focused only on observations in winter for four reasons. First, summer CO shows greater instability as its atmospheric lifetime depends on OH radical production, which is enhanced through photochemical reactions (e.g., CH_4 oxidation) under intense solar radiation, making CO a less reliable fossil fuel tracer (Rosendahl, 2022). Second, winter exhibits stronger ΔCO-C_{ff} correlations ($r > 0.6$, $p < 0.01$; Fig. H2) with better regional representativeness due to extended CO atmospheric lifetime from slower CO oxidation rates. Third, the winter ΔCO-C_{ff} relationship better captures anthropogenic emission characteristics compared to other seasons. Fourth, weaker vertical mixing in winter accentuates local emission impacts (Wang et al., 2010).

We then estimated winter 2022 $R_{CO/CO2ff}$ ratios across Chinese cities using ΔCO-C_{ff} regression slopes (Fig. H2), with spatial variations primarily attributed to differences in fuel composition and combustion efficiency (Graven et al., 2009). CO is generated through incomplete combustion of both fossil fuels and biomass. These spatial patterns are consistent with combustion characteristics showing biomass burning produces higher CO emissions per unit energy than fossil fuel combustion (Akagi et al., 2011). As shown in Fig. H1, suburban/rural sites (GZ1, SZ9, ZJ1, SG1) exhibited significantly higher ratios than urban sites (GZ5, SZ7, ZJ4, SG3): GZ1 > GZ5 ((30.4 ± 10.0) > (19.8 ± 4.6) nmol μmol^{-1}), SZ9 > SZ7 ((41.3 ± 23.0) > (14.8 ± 2.4) nmol μmol^{-1}), ZJ1 > ZJ4 ((41.2 ± 3.6) > (11.9 ± 6.4) nmol μmol^{-1}), and SG1 > SG3 ((26.7 ± 2.9) > (15.1 ± 3.6) nmol μmol^{-1}). This pattern is in agreement with previous studies attributing elevated ratios in non-urban

https://doi.org/10.5194/egusphere-2025-1931
Preprint. Discussion started: 25 June 2025

areas to biomass burning contributions (Rosendahl, 2022). In contrast, megacities showed 35–40 % lower ratios (Guangzhou: 13.3 nmol μmol^{-1}, Shenzhen: 14.1 nmol μmol^{-1}) compared to smaller cities (Zhanjiang: 21.3 nmol μmol^{-1}, Shaoguan: 21.7 nmol μmol^{-1}; $p < 0.01$; Fig. H2), suggest higher fossil fuel combustion efficiency and/or lower biomass burning inputs. Guangzhou's ratios are dominated by improved fossil fuel combustion efficiency due to having the highest biomass burning emissions among the four studied cities in the EDGAR2024 inventory, while Shenzhen's ratios are attributed to both factors with nearly negligible biomass contributions corresponding to its 2017 biomass boiler phase-out policy.

We retrieved historical $R_{CO/CO2ff}$ data from observations in China by estimation from $\Delta(^{14}C)$ measurements and correction from $R_{CO/CO2}$ (increased by 20 %) (Table H1), and $I_{CO/CO2ff}$ data from the MEIC, MIXv2, and EDGAR inventories (Fig. 6). Given the minor contribution of biomass burning (BB)-related CO emissions across all inventories, with $I_{CO/CO2ff}$ ratio below 0.003 (MEIC, incorporating OBBEIC data (Song et al., 2009; Huang et al., 2012)), less than 1.0 (MIXv2), and declining from 3.8 (1990) to 1.1 (2022) in EDGAR, we assume that interannual variability in BB emissions has negligible influence on the overall emission ratios. Observational and inventory data show a sustained decline in China's $R_{CO/CO2ff}$ and $I_{CO/CO2ff}$ ratios over the past 30 years (Fig. 6a), demonstrating that efforts to improve fossil fuel combustion efficiency are effective (Wang et al., 2010; Lee et al., 2020), which is another factor contributing to the reduction in C_{ff} concentrations. The MEIC inventory attributes this trend to spatiotemporally heterogeneous mitigation pathways: 72 % of the cities started $I_{CO/CO2ff}$ reductions during 1990–1994, while the remaining 28 % (mainly concentrated in the western provinces) exhibited a delayed start until 1995–2004. The implementation of China's clean air policies since 2013 has systematically phased out small, inefficient combustion facilities and replaced them with centralized, high efficient, and clean energy infrastructure (Shi et al., 2022). The phase-out of coal-fired industrial boilers during 2013–2020 reduced CO_2 emissions by (1.5 ± 0.3) Gt, accounting for 12 % of the national industrial emission reduction (Li, 2023). These technological transitions enhanced combustion efficiency by >10 %, and reduced coal-dominated energy intensity by 40 % across the sector. The MEIC inventory showed that these synergistic measures resulted in significant energy savings, with a net reduction of 0.25 gigatonnes of coal equivalent (Gtce) in 2020 and a cumulative reduction of 1.06 Gtce over the policy implementation period (Shi et al., 2022). Critically, the efficiency-driven transition decoupled energy demand from C_{ff} emissions, with combustion optimization directly reducing coal consumption 1–2 % and C_{ff} emissions by 1–3 Gt per year after 2015 (Le Quéré et al., 2016; Friedlingstein et al., 2023a).

We systematically compared observational $R_{CO/CO2ff}$ values with inventory $I_{CO/CO2ff}$ estimates. Our 2022 measurements of the $R_{CO/CO2ff}$ ratios in megacities (Guangzhou and Shenzhen) were consistent with EDGAR estimates (14.9 nmol μmol^{-1}, 2022), while those in smaller cities (Zhanjiang and Shaoguan) were closer to MEIC values (19.2 nmol μmol^{-1}, 2020) (Fig. 6a) and independent field measurements near Xi'an (23 ± 6 nmol μmol^{-1}, 2021) (Liu et al., 2024). City comparisons of observations against MEIC estimates revealed systematic deviations: Shenzhen's observed ratio fell 24 % below inventory estimates (23.4 nmol μmol^{-1}), whereas Shaoguan's exceeded projections (12.7 nmol μmol^{-1}) by 38 %; Guangzhou's and Zhanjiang's are similar to inventory estimates (14.2 and 23.8 nmol μmol^{-1}, respectively) (Fig. 6b).

https://doi.org/10.5194/egusphere-2025-1931
Preprint. Discussion started: 25 June 2025

The three-decade observational $R_{CO/CO2ff}$ ratios are closer to (higher than) the MEIC estimates with a difference of (22 ± 23) % compared with the MIXv2 and EDGAR estimates, when focusing on the ratios over time and ignoring the local deviations caused by the specific cities. These findings indicate that the MEIC inventory is more accurate than the EDGAR inventory for China. For specific cities, we found that the MEIC inventory estimates were deviated less from the observed $R_{CO/CO2ff}$ (based on $\Delta(^{14}C)$ measurements) in recent years than the corrected $R_{CO/CO2ff}$ (using $R_{CO/CO2}$) in earlier years for Beijing and Guangzhou (Fig. 6b). For example, in Beijing, the discrepancy in the ratios between observations and inventories decreased from 22 % in 2006–2007 ($R_{CO/CO2}$-corrected) (Wang et al., 2010) to 8.7 % in 2009–2010 ($\Delta(^{14}C)$-derived) (Turnbull et al., 2011), and further declined to 7.0 % by 2014 ($\Delta(^{14}C)$-derived) (Niu et al., 2018). Similarly, in Guangzhou, the discrepancy dropped from 84 % in 2009–2010 ($R_{CO/CO2}$-corrected) (Silva et al., 2013) to 34 % in 2014–2017 ($R_{CO/CO2}$-corrected) (Mai et al., 2021), and eventually reached 6.4 % by 2022 ($\Delta(^{14}C)$-derived). These results suggest that $R_{CO/CO2}$ corrections should be carefully interpreted, as the effect of CO_2 from non-fossil sources can significantly bias the results, even in megacities with high C_{ff} emissions. For example, human respiration could bias $R_{CO/CO2}$ low by about 9 % at a rural site near Beijing (Wang et al., 2010; Turnbull et al., 2011).

Despite the relatively good agreement of ratios between observations ($R_{CO/CO2ff}$) and MEIC inventory ($I_{CO/CO2ff}$) at the national scale, observational data exhibited significantly greater $R_{CO/CO2ff}$ reduction rates than inventory estimates when examined at the city level. From observations (Fig. 6b), in Guangzhou, $R_{CO/CO2ff}$ decreased by 36 % from 35.8 nmol μmol^{-1} in 2009–2010 (Silva et al., 2013) to 23.8 nmol μmol^{-1} in winter of 2014–2017 (Mai et al., 2021) and by 63 % to 13.3 nmol μmol^{-1} in 2022; in Beijing, $R_{CO/CO2ff}$ decreased by 58 % from72.3 nmol μmol^{-1} in 2004 (Han et al., 2009) to 30.4 nmol μmol^{-1} in 2014 (Niu et al., 2018); in Xi'an, $R_{CO/CO2ff}$ decreased by 50 % from (46 ± 13) nmol μmol^{-1} in 2016 (Wang et al., 2018) to (23 ± 6) nmol μmol^{-1} in 2021 (Liu et al., 2024). The MEIC estimates for the above three cities decreased by 36 %, 52 %, and 21 %, respectively, over the same period. Larger reductions of the ratios were found from observations than those from the MEIC inventory (i.e., 63 % > 36 % for Guangzhou, 58 % > 52 % for Beijing, and 50 % > 21 % for Xi'an). This conclusion holds even after artificially biasing the $R_{CO/CO2ff}$ ratio downward by about 9 % to account for human respiration in Beijing (2004) and in Guangzhou (2009–2010 and 2014–2017). These findings suggest that the MEIC inventory may insufficiently capture, or lag, the rapid improvement in combustion efficiency and energy structure transformation in China.

The three-decade decline in China's $R_{CO/CO2ff}$ ratios demonstrates both improved fossil fuel combustion efficiency and successful implementation of air pollution control policies i.e., the success of air pollution emission reduction efforts. Our observations reveal significantly greater urban $R_{CO/CO2ff}$ reductions than those estimated by the MEIC inventory, indicating potential underestimation of CO emission reductions relative to C_{ff} mitigations in current inventories. This finding aligns with previous reports of inventory underestimates for real-world CO reductions. Mai et al. (2021) showed that the MEIC inventory may underestimate cumulative reductions from fleet turnover and catalytic converter upgrades, despite China's National V standards having achieved the ≤1 g km^{-1} CO emission limit since 2013. Together, these results imply that the MEIC inventory might systematically underestimate the actual effectiveness of clean air policies in reducing air pollutant emissions.

https://doi.org/10.5194/egusphere-2025-1931
Preprint. Discussion started: 25 June 2025

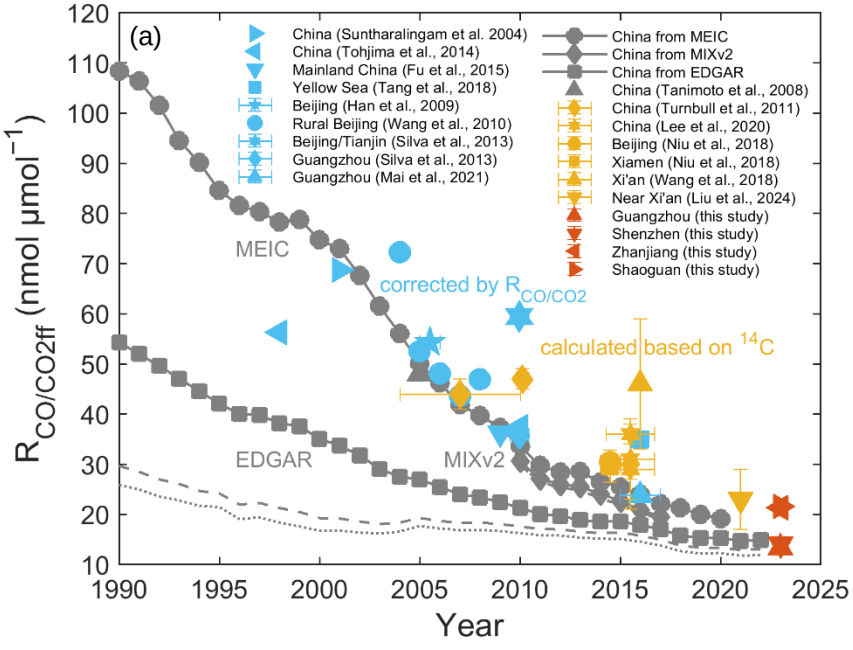

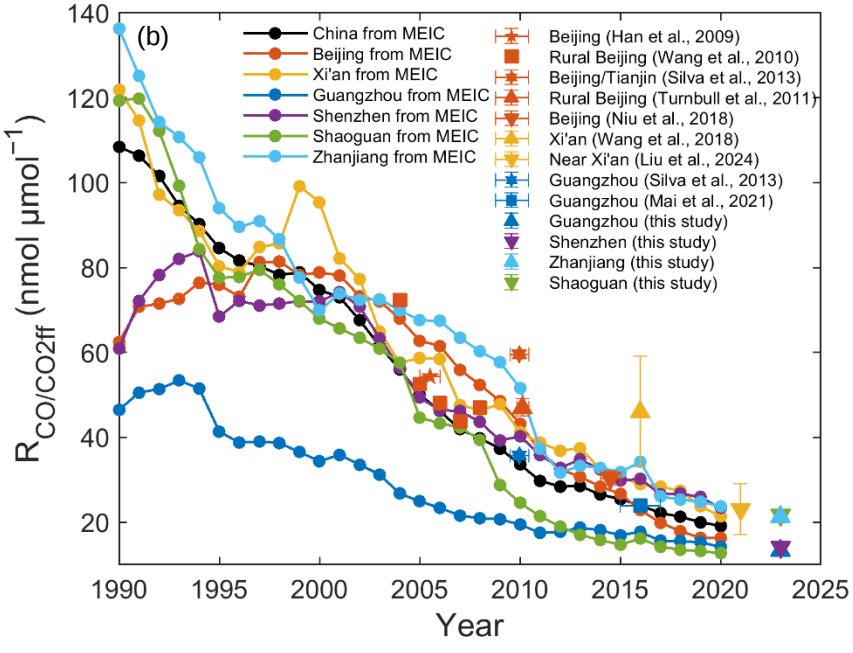

Figure 6: $R_{CO/CO2ff}$ for (a) China and for (b) Chinses cities obtained from inventories and observations (values refer to Table H1). For (a), the gray symbols represent data from the emission inventories (Tanimoto et al., 2008), including MEIC (Meic, 2023; Xu et al., 2024; Li et al., 2019; Li et al., 2017), MIXv2 (Li et al., 2024), and EDGAR2024 (Edgar, 2024). The $I_{CO/CO2ff}$ emission ratios

https://doi.org/10.5194/egusphere-2025-1931
Preprint. Discussion started: 25 June 2025

derived from the three inventories are shown with distinct approaches: (1) MEIC calculated the $I_{CO/CO2ff}$ ratio for all anthropogenic sectors (represented by solid line with point symbols); (2) MIXv2 computed two variants: combining anthropogenic sectors with open biomass burning (solid line with diamond symbols) and anthropogenic-only emissions (dash-dotted line); while (3) EDGAR2024 provided three ratios: fossil + biogenic CO (solid line with square symbols), fossil + biomass burning CO (dashed line), and fossil-only CO (dotted line), all relative to C_{ff} emissions. The light blue symbols represent $R_{CO/CO2ff}$ corrected by $R_{CO/CO2}$ from observational studies (Wang et al., 2010; Tohjima et al., 2014; Suntharalingam et al., 2004; Tang et al., 2018; Han et al., 2009; Fu et al., 2015), assuming that 20 % of the CO_2 enhancement was from sources other than C_{ff}. The orange symbols represent $R_{CO/CO2ff}$ calculated based on atmospheric $^{14}CO_2$ measurements from previous studies (Turnbull et al., 2011; Niu et al., 2018; Lee et al., 2020; Wang et al., 2018; Liu et al., 2024). The red symbols depict the values observed in this study. For (b), the Chinese cities include Beijing, Xi'an, Guangzhou, Shenzhen, Zhanjiang, and Shaoguan from the MEIC inventory (filled circles) and observations from previous studies (Wang et al., 2018; Liu et al., 2024; Wang et al., 2010; Silva et al., 2013; Niu et al., 2018; Mai et al., 2021; Han et al., 2009; Turnbull et al., 2011) and this study since 1990. The up and down triangles represent $R_{CO/CO2ff}$ estimated based on atmospheric $\Delta(^{14}CO_2)$ measurements. Other symbols represent the $R_{CO/CO2ff}$ corrected by $R_{CO/CO2}$ from observational studies, assuming that 20 % of the CO_2 enhancement is from sources other than C_{ff}. The y-axis error bars indicate uncertainty, and the x-axis error bars represent the observed period.

3.6 Implication

Since 2013, China has implemented a series of measures with the explicit aim of improving air quality. While the initial goal of China's clean air targets was to address air pollution, they also served as a powerful catalyst for the simultaneous transformation of energy systems and the mitigation of C_{ff} emissions. As a result, we have observed C_{ff} concentration and emission reductions in some Chinese megacities and supercities, such as Guangzhou, Beijing, and Xi'an. The achievement of peak emissions in Beijing (2010) and Xi'an (2013) marks a pivotal transition for China, signaling that cities across the nation, from megacities to small cities, are gradually reaching their emission peaks. This milestone has profound implications for both China's sustainable development and global climate governance, as China has dominated the global trend since 2010 (Friedlingstein et al., 2023b).

Despite China's remarkable success in reducing C_{ff} emissions, continued efforts are needed to optimize the nation's energy system and economic structure in order to facilitate future green growth. It is imperative that common solutions to climate change and air pollution are formulated and implemented with urgency, as China has set a goal for all cities to meet current air quality standards by 2035 and has pledged to achieve carbon peak by 2030 and carbon neutrality by 2060. One available solution is to control the common key sources and dominant source regions of air pollution and CO_2 emissions (Wu et al., 2022; Zheng et al., 2024). In future policymaking, it is essential to adopt a co-beneficiary strategy that co-ordinates clean air measures and addresses climate change measures. This strategy, together with the associated assessment approach, will be an essential part of achieving sustainable development.

4 Conclusions

This study advances the understanding of urban C_{ff} concentration changes in China through three key contributions. First, we pioneer the integration of biomass burning emissions into C_{ff} estimation frameworks, significantly improving

https://doi.org/10.5194/egusphere-2025-1931
Preprint. Discussion started: 25 June 2025

methodological accuracy. Second, we identify substantial C_{ff} reductions in cities and their source regions, driven by coal-to-gas transitions (evidenced by stable isotope analysis) and combustion efficiency improvements (confirmed by declining $R_{CO/CO2ff}$ ratios), where megacities and supercities lead this decline. Finally, through systematic analysis of long-term $R_{CO/CO2ff}$ trends, we reveal current emission inventories may underestimate combustion efficiency gains and CO emission reductions relative to C_{ff} mitigations. These findings provide critical support for refining emission accounting systems and developing evidence-based climate policies. The integrated approach offers new insights into urban emission dynamics and mitigation effectiveness.

This study has some limitations in sampling and source attribution. First, current sampling only covers summer and winter; future work should include all seasons to better capture annual trends. Second, the $\delta(^{13}C)$ signatures used here mainly rely on published data, introducing potential uncertainties. Direct measurements of source-specific isotopic values would help refine the analysis. Additionally, future studies could incorporate atmospheric modelling and inversion methods to improve emission estimates. This would require high resolution prior flux data and validation against direct measurements (e.g., radiocarbon analysis). Addressing these gaps would enhance source apportionment accuracy and enable a more robust integration of top-down (e.g., inversions) and bottom-up (e.g., inventories) approaches for evaluating urban emission mitigation strategies.

https://doi.org/10.5194/egusphere-2025-1931
Preprint. Discussion started: 25 June 2025

Appendix A: Seasonal averages and quality control of $\Delta(^{14}C)$ and $\delta(^{13}C)$ measurements

Table A1 $\Delta(^{14}C)$ and $\delta(^{13}C)$ averages and standard deviations at 30 sampling sites

City	Site code	Summer		Winter		Altitude (m a.s.l.)	Elevation (m a.g.l.)	Site description
		$\Delta(^{14}C)$ (‰)	$\delta(^{13}C)$ (‰)	$\Delta(^{14}C)$ (‰)	$\delta(^{13}C)$ (‰)			
Guangzhou	GZ1	−15.3 ± 9.8	−9.0 ± 0.7	−37.6 ± 8.2	−8.9 ± 0.2	212	25	Suburban rooftops
	GZ2	−21.7 ± 4.8	−9.0 ± 0.3	−48.4 ± 5.6	−8.9 ± 0.3	19	20	Suburban rooftops
	GZ3	−16.4 ± 8.9	−8.7 ± 0.3	−38.0 ± 4.0	−8.7 ± 0.2	120	30	Suburban rooftops
	GZ4	−16.1 ± 4.8	−9.0 ± 0.7	−41.3 ± 9.4	−9.0 ± 0.3	23	35	Urban rooftops
	GZ5	−34.3 ± 12.4	−9.6 ± 0.8	−39.6 ± 8.3	−8.5 ± 0.3	46	35	Urban rooftops
	GZ6	−33.7 ± 16.8	−9.5 ± 1.0	−44.4 ± 11.3	−8.9 ± 0.1	53	60	Urban rooftops
	GZ7	−17.0 ± 5.1	−8.8 ± 0.4	−39.6 ± 7.3	−8.9 ± 0.3	120/ 75	118/ 40	Urban tower/ Urban rooftops
	GZ8	−24.4 ± 9.5	−9.4 ± 0.5	−41.2 ± 8.1	−9.2 ± 0.2	12	30	Urban rooftops
	GZ9	−27.4 ± 5.4	−9.8 ± 0.4	−42.7 ± 7.0	−8.7 ± 0.3	50	30	Urban rooftops
	GZ10	−26.6 ± 20.0	−9.5 ± 1.0	−42.8 ± 5.9	−9.0 ± 0.2	54	40	Suburban rooftops
Shenzhen	SZ1	−14.9 ± 18.1	−8.6 ± 0.5	−38.0 ± 27.3	−9.2 ± 0.2	40	30	Suburban tower
	SZ2	−55.2 ± 3.9	−9.2 ± 0.4	−43.5 ± 9.0	−9.4 ± 0.1	28	15	Rooftops in Industrial area
	SZ3	−12.3 ± 22.7	−8.7 ± 0.5	−48.0 ± 16.2	−9.4 ± 0.3	14	15	Urban rooftops
	SZ4	−15.2 ± 28.1	−8.8 ± 0.6	−45.3 ± 15.3	−9.5 ± 0.3	42	40	Urban campus rooftops
	SZ5	−17.9 ± 17.7	−8.8 ± 0.3	−42.1 ± 12.5	−9.4 ± 0.3	40	30	Urban campus rooftops
	SZ6	−17.3 ± 10.4	−8.7 ± 0.5	−43.1 ± 32.2	−9.1 ± 0.4	60	30	Suburban tower
	SZ7	−11.3 ± 6.1	−8.8 ± 0.1	−40.3 ± 33.5	−9.3 ± 0.6	210	200	Urban rooftops
	SZ8	−9.8 ± 12.8	−8.6 ± 0.5	−35.5 ± 32.0	−9.0 ± 0.3	150	110	Suburban rooftops at the boundary site
	SZ9	−4.5 ± 11.6	−8.5 ± 0.4	−36.8 ± 32.3	−9.2 ± 0.3	60	30	Suburban tower
	SZ10	1.9 ± 1.9	−9.0 ± 0.8	−44.4 ± 7.8	−9.4 ± 0.2	60	20	Suburban rooftops
Zhanjiang	ZJ1	−10.5 ± 9.5	−10.2 ± 0.5	−27.3 ± 13.0	−9.1 ± 0.4	8	20	Rural rooftops
	ZJ2	−15.0 ± 14.7	−9.5 ± 0.6	−27.1 ± 12.7	−9.0 ± 0.2	24	40	Urban rooftops
	ZJ3	−9.8 ± 4.9	−10.2 ± 0.6	−28.6 ± 12.8	−9.1 ± 0.1	44	40	Urban rooftops
	ZJ4	−5.6 ± 7.1	−8.9 ± 0.3	−30.3 ± 12.4	−9.1 ± 0.2	25	40	Urban rooftops
	ZJ5	−14.6 ± 13.7	−8.8 ± 0.2	−31.9 ± 11.8	−9.4 ± 0.4	41/ 46	50/ 30	Suburban campus site/ Site near the port area
Shaoguan	SG1	−15.9 ± 16.1	−8.9 ± 0.3	−11.7 ± 5.2	−9.0 ± 0.1	114	30	Suburban rooftops
	SG2	−20.7 ± 15.2	−9.5 ± 0.3	−19.7 ± 3.8	−8.9 ± 0.2	60	40	Urban campus rooftops
	SG3	−18.0 ± 17.5	−9.2 ± 0.5	−26.6 ± 10.4	−9.0 ± 0.2	68	40	Urban rooftops
	SG4	−35.2 ± 21.0	−9.0 ± 0.2	−11.1 ± 6.3	−8.8 ± 0.2	95	30	Rural site
	SG5/ NL	5.1 ± 1.3	−9.2 ± 0.2	−2.0 ± 0.8	−9.3 ± 0.2	1700	15	Rooftops at the background site

https://doi.org/10.5194/egusphere-2025-1931
Preprint. Discussion started: 25 June 2025

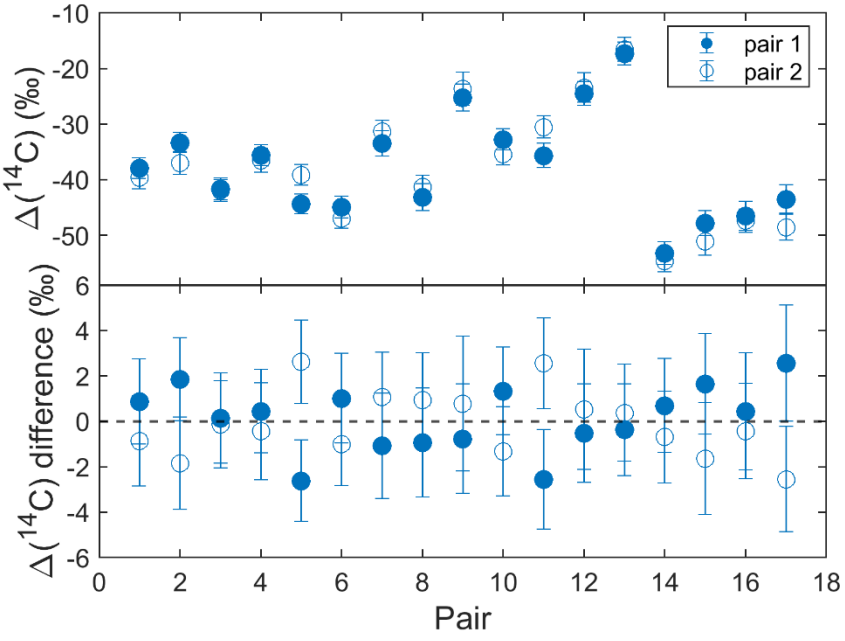

Figure A1 Pair differences of $\Delta(^{14}C)$ for replicate measurements. Replicates were obtained from parallel air samples. The difference of each individual measurement from its pair mean is shown. Closed and open symbols are the first and second group taken from each pair, respectively. Error bars are the 1-sigma uncertainty on each measurement.

Appendix B: Radiocarbon isotope endmembers for biomass burning

Atmospheric $^{14}CO_2$ is assimilated by plants via photosynthesis, imprinting atmospheric $\Delta(^{14}CO_2)$ signatures into plant tissues. This creates a bidirectional link: plant $\Delta(^{14}C)$ reflects atmospheric $\Delta(^{14}CO_2)$ levels, while atmospheric $\Delta(^{14}CO_2)$ dynamics can be inferred from plant biomass archives (e.g., tree rings). Annual biomass $\Delta(^{14}C)$ closely matches contemporaneous atmospheric $\Delta(^{14}CO_2)$ (due to rapid carbon turnover within a single growing season). Multi-year biomass $\Delta(^{14}C)$ represents an integrated signal, blending atmospheric $\Delta(^{14}CO_2)$ variations over its growth period (e.g., tree rings capture annual $\Delta(^{14}CO_2)$ fluctuations).

B1 Annual biomass. The $\Delta(^{14}C)$ for annual biomass in 2022 was estimated as −14.8 ± 2.2 ‰ (mean ± MSE; Δ_a), derived from a linear regression model of atmospheric $\Delta(^{14}CO_2)$ decline (−4.4 ‰ a^{-1}) observed in Northern Hemisphere zone 3 between 2010 and 2018 (Hua et al., 2021).

B2 Multi-year biomass. The $\Delta(^{14}C)$ for multi-year biomass is related with its age; the year it was growing, the annual increase in biomass, and atmospheric $^{14}CO_2$ during its growth cycle. The $\Delta(^{14}C)$ for multi-year biomass can be determined (Lewis et al., 2004):

https://doi.org/10.5194/egusphere-2025-1931
Preprint. Discussion started: 25 June 2025

$$\Delta^{14}C = \frac{\int_{t_1}^{t_2} \Delta^{14}C(t)w(t)dt}{\int_{t_1}^{t_2} w(t)dt} \quad \text{(B1)}$$

where $\Delta^{14}C(t)$ is the atmospheric $\Delta(^{14}CO_2)$ at age t, and the weighting function w(t) is the growth rate of carbon in biomass at age t, which can be determined by the Chapman-Richards growth model (Lewis et al., 2004):

$$V = A(1 - e^{-\frac{t-t_0}{\tau}})^m \quad \text{(B2)}$$

$$w(t) = \frac{dV}{dt} \quad \text{(B3)}$$

where V is the volume of a tree at age t ($V = 0$ at $t = t_0$), and the parameters A, τ, and m can be chosen empirically to fit measured tree growth characteristics. The Chapman-Richards growth model describes cumulative growth of V.

It is assumed that the multi-year biomass was partitioned into five age cohorts (10-, 20-, 40-, 65-, and 85-year-old trees) with relative share of 20 ± 10 %, 20 ± 10 %, 40 ± 20 %, 10 ± 5 % and 10 ± 5 %, respectively (Mohn et al., 2008). The corresponding $\Delta(^{14}C)$ values were calculated as 20.9 ± 5.4 ‰, 52.9 ± 4.0 ‰, 137.5 ± 35.1 ‰, 261.2 ± 50.4 ‰, and 203.1 ± 17.4 ‰, respectively. Consequently, the $\Delta(^{14}C)$ signature of the multi-year biomass for the year 2022 was estimated as 116.2 ± 17.6 ‰ (mean ± 1σ; Δ_m) using the Chapman-Richards growth model ($\tau = 50, m = 3$) and long-term tree-ring $\Delta(^{14}C)$ measurements (Hua et al., 2021).

B3 Biomass burning. The $\Delta(^{14}C)$ endmember for biomass burning (Δ_{BB}) was calculated using the two biomass types:

$$\Delta_{BB} = f_a \cdot \Delta_a + (1 - f_a) \cdot \Delta_m \quad \text{(B4)}$$

where Δ_a and Δ_m represent the $\Delta(^{14}C)$ signatures of annual biomass (e.g., crop residues) and multi-year biomass (e.g., woody waste), respectively, and f_a is the annual biomass fraction.

Using this framework, we estimated the 2022 $\Delta(^{14}C)$ endmembers for biomass burning as 116.2 ± 17.6 ‰, 103.1 ± 15.8 ‰, 90.0 ± 14.1 ‰, 76.9 ± 12.3 ‰, 63.8 ± 10.6 ‰, and 50.7 ± 8.9 ‰ for f_a values of 0 %, 10 %, 20 %, 30 %, 40 %, 50 %, respectively.

Appendix C: Bias correction for C_{ff} calculation

C1 Nuclear facilities. All operational (Daya Bay, Ling'ao, Yangjiang, Taishan) and under-construction (Lufeng, Taipingling, Lianjiang) nuclear power plants (NPPs) along the coastline of Guangdong Province employ pressurized water reactor (PWR) technology. Airborne ^{14}C releases from these facilities are predominantly hydrocarbons (75–95 %), mainly CH_4, with only a small fraction in the form of CO_2 (Iaea, 2004). In fact, almost all reactors in China (> 95 %) are the PWR type, which has the lowest emission factor for $^{14}CO_2$ release (Graven and Gruber, 2011; Yang, 2024). Graven and Gruber (2011) note that most of China and the western US are the areas with very little potential bias in the derived C_{ff}, owing to intense fossil fuel emissions but little to no nuclear activity. Graven et al. (2018) confirm this view that emissions from reactors in the western US have a negligible effect on their samples, simulating an effect on inferred C_{ff} of less than 0.1 ppm. Although we can't obtain the $\Delta(^{14}CO_2)$ emission monitoring data from NPPs in China, *National Report on Radiation*

https://doi.org/10.5194/egusphere-2025-1931
Preprint. Discussion started: 25 June 2025

Environment Quality confirms that no incidents of excessive radiation dose discharges have occurred at NPPs in Guangdong Province. For example, data from 2011 to 2014 show that liquid radionuclide discharges from Daya Bay and Ling'ao NPPs were only 0.09–0.38 % of legal thresholds. The 2019 report highlighted that public radiation doses at NPPs such as Daya Bay and Taishan remained "significantly below regulatory limits" (Meec, 2021). We thus assume that the $^{14}CO_2$ effect from the NPPs in Guangdong Province may also be negligible, referred to the results from the western US and Chinese regulatory standards for radioactive discharges from NPPs.

C2 Biospheric exchange. Biospheric carbon fluxes associated with photosynthesis, autotrophic respiration, and annual biomass burning generally do not alter atmospheric $\Delta(^{14}C)$ levels, as the carbon exchanged through these processes largely maintains isotopic equilibrium with contemporary atmospheric CO_2 (Turnbull et al., 2009). In contrast, heterotrophic respiration and multi-year biomass burning (e.g., wildfire consuming legacy organic matter) release carbon fixed during periods of elevated atmospheric $\Delta(^{14}C)$, such as the 1960s nuclear bomb testing peak. This temporal decoupling between carbon uptake and release introduces a measurable positive bias in modern $\Delta(^{14}C)$, reflecting the delayed contribution of older carbon pools. Therefore, we use estimates of heterotrophic respiration (Rh) and biomass burning (BB) fluxes to correct for biospheric influence on C_{ff} calculation.

C2.1 Heterotrophic respiration. The heterotrophic respiration correction term (β_{Rh}) is calculated by the following equation:

$$\beta_{Rh} = \frac{C_{Rh}(\Delta_{bg}-\Delta_{Rh})}{\Delta_{bg}+1000‰} \quad \text{(C1)}$$

where C_{Rh} is the CO_2 mole fraction estimated by coupling hourly FLEXPART footprints with the heterotrophic respiration fluxes extracted from the Carnegie Ames Stanford Approach Global Fire Emissions Database Version 4 (CASA-GFED4s) (Randerson et al., 2017; Van Der Werf et al., 2017). We imposed the diurnal cycle from the CASA-GFED3 (Van Der Werf et al., 2010) heterotrophic respiration fluxes (estimated as half of the ecosystem respiration, which is calculated as the difference between net ecosystem exchange and gross ecosystem exchange; [NEE − GEE]/2) onto the nearest neighbor CASA-GFED4s monthly mean fluxes to approximate hourly resolved fluxes. By aggregating these flux estimates, we created flux maps matching the spatial resolution of the hourly FLEXPART footprints. We then calculated C_{Rh} by multiplying the FLEXPART footprints with heterotrophic respiration flux maps. The simulated C_{Rh} concentrations were 1.5 ± 0.7 μmol mol^{-1} (range: 0.5−3.1 μmol mol^{-1}) in summer and 2.2 ± 0.9 μmol mol^{-1} (range: 0.4−3.8 μmol mol^{-1}) in winter. We used a value of 40 ± 35 ‰ for the $\Delta(^{14}CO_2)$ signature of heterotrophic respiration (Δ_{Rh}), based on the value of 75 ± 35 ‰ in 2015 (Graven et al., 2018) and considering a decrease of 5 ‰ per year (Zazzeri et al., 2023). The disequilibrium correction from heterotrophic respiration (β_{Rh}) were estimated to be –0.06 ± 0.03 ppm (range: –0.14 to –0.02 ppm) in summer and –0.11 ± 0.04 ppm (range: –0.20 to –0.02 ppm) in winter.

C2.2 Biomass burning. For the influence from biomass burning, we extracted CO_2 emissions from biomass burning in Guangdong Province and four cities from the CASA-GFED4s (Randerson et al., 2017; Van Der Werf et al., 2017), and C_{bio} emissions from the Emissions Database for Global Atmospheric Research (EDGAR) (Edgar, 2024). Key methodological distinctions arise from the differing scopes of these datasets: CASA-GFED4s quantifies open-environment fires (i.e.,

https://doi.org/10.5194/egusphere-2025-1931
Preprint. Discussion started: 25 June 2025

satellite-observable combustion events including wildfires, agricultural residue burning, savanna/rangeland fires, and small fires), whereas EDGAR also incorporates emissions from closed-system combustion (e.g., industrial or residential biomass use).

Biomass burning emissions from CASA-GFED4s accounted for <2 % of Rh emissions across Guangdong Province and the four studied cities. In contrast, EDGARv2024ghg C_{bio} estimates represented a substantially higher proportion of Rh emissions, ranging from 7–29 % (Guangdong), 24–92 % (Guangzhou), 16–97 % (Shenzhen), 13–38 % (Zhanjiang), to 73–248 % (Shaoguan). Given the small disequilibrium corrections for Rh, the simulated contribution of BB emissions to C_{ff} estimates was negligible when using CASA-GFED4s data. However, EDGAR-derived C_{bio} scenarios indicated a potentially higher influence on C_{ff} quantification, particularly in regions with high biomass combustion activity.

To estimate the biomass burning correction term (β_{BB}) using the EDGAR2024 C_{bio} inventory (Edgar, 2024), we first derived total C_{BB} simulations (C_{BB}) by applying a biomass burning fraction (α_{BB}) to the C_{bio} simulations (C_{bio}). This parameter α_{BB} represents the proportion of C_{bio} emissions attributable to biomass burning:

$$C_{BB} = C_{bio} \cdot \alpha_{BB} \quad \text{(C2)}$$

The correction term β_{BB} was subsequently calculated as:

$$\beta_{BB} = \frac{C_{BB}(\Delta_{bg} - \Delta_{BB})}{\Delta_{bg} + 1000‰} \quad \text{(C3)}$$

For simulated C_{bio} mole fraction estimation in 2022, we implemented a three-stage process: (1) Generating 0.1°×0.1° resolution flux maps through integration of EDGAR2024 C_{bio} emission fluxes with FLEXPART atmospheric transport footprints, (2) performing spatiotemporal aggregation to align with FLEXPART model output specifications, and (3) calculating concentrations via convolution operations between transport footprints and optimized flux fields.

We adopted $\Delta(^{14}CO_2)$ signatures of −14.8 ± 2.2 ‰ (annual biomass burning) and 116.2 ± 17.6 ‰ (multi-year biomass burning) calculated in Appendix B. For 2022 $\Delta(^{14}C)$ endmembers for biomass burning, we estimated values of 116.2 ± 17.6 ‰ (0 % annual biomass), 103.1 ± 15.8 ‰ (10 %), 90.0 ± 14.1 ‰ (20 %), 76.9 ± 12.3 ‰ (30 %), 63.8 ± 10.6 ‰ (40 %), and 50.7 ± 8.9 ‰ (50 %), corresponding to incremental annual biomass burning fractions from 0 % to 50 %.

We quantified disequilibrium correction terms under the maximum biomass burning (BB) contribution scenario (f_a = 0 % and α_{BB}=100 %). The simulated C_{BB} concentrations were 0.8 ± 0.7 μmol mol^{-1} (range: 0.0−1.9 μmol mol^{-1}) in summer and 1.9 ± 1.0 μmol mol^{-1} (range: 0.1−4.4 μmol mol^{-1}) in winter. The BB-specific correction term (β_{BB}) exhibited seasonal variations: −0.09 ± 0.08 μmol mol^{-1} (range: −0.46 to −0.01 μmol mol^{-1}) in summer and −0.24 ± 0.12 μmol mol^{-1} (range: −0.56 to −0.02 μmol mol^{-1}) in winter under 0 % annual biomass burning contribution. The combined correction factor β, integrating contributions from both heterotrophic respiration (Rh) and biomass burning (BB), showed broader ranges: −0.16 ± 0.09 μmol mol^{-1} (range: −0.55 to −0.03 μmol mol^{-1}) in summer and −0.35 ± 0.15 μmol mol^{-1} (range: −0.72 to −0.04 μmol mol^{-1}) in winter.

https://doi.org/10.5194/egusphere-2025-1931
Preprint. Discussion started: 25 June 2025

Appendix D: Background selection

As we summarized in Zhou et al. (2024), Turnbull et al. (2015) concluded that for Indianapolis, a city with relatively simple boundary conditions, the upwind background site (Tower 1) is more appropriate compared with continental and regional background sites (LEF and NWR). In contrast, for Los Angeles, a city with relatively complex boundary conditions, Newman et al. (2016) and Miller et al. (2020) tend to use the neighboring regional or continental background sites (MWO and LJO; BRW and NWR), because the upwind background within the city may be influenced by emissions from neighboring cities and therefore cannot represent the local urban background. In this study, the cities concerned are central cities or neighboring cities of the Pearl River Delta (PRD) urban agglomeration with relatively complex boundary conditions, so we chose the nearest regional background site NL (i.e., SG5) as the background for determining the C_{ff} concentrations.

The Nanling site serve as an ideal site for Guangdong's atmospheric background monitoring station due to its remote location (over 100 km from the PRD urban agglomeration), high-altitude terrain (>1,000 m) avoiding localized pollution, and strategic position as a climate/watershed boundary intercepting seasonal airflows, collectively enabling precise monitoring of regional atmospheric transport patterns while meeting strict background station criteria for pollution isolation and cross-boundary impact assessment.

On the other hand, the "annual" CO_2 and $\Delta(^{14}C)$ averages at NL, which are close to those at the Jungfraujoch, are positioned in the upper-right section of the Keeling plot of $\Delta(^{14}C)$ and CO_2 representing the background, by comparison with the values at the Waliguan (Fig. 3). Additionally, the $\Delta(^{14}C)$ and CO_2 averages at NL were the highest and the lowest among the 30 sampling sites, respectively (Table A1), which are consistent with background-level criteria.

https://doi.org/10.5194/egusphere-2025-1931
Preprint. Discussion started: 25 June 2025

Appendix E: Comparison of C_{ff} fractions and concentrations among various cities

Table E1 Comparison of C_{ff} and C_{bio} fractions derived from $\Delta(^{14}CO_2)$ measurements in various cities

City	Time	Background	C_{ff} (%)	C_{bio} (%)	References
Paris	2010	MHD [a]	77	23	(Lopez et al., 2013)
Los Angeles	2006-2013 winter	LJO [b]	86	14	(Newman et al., 2016)
Los Angeles	2006-2013 summer	LJO	93	7	(Newman et al., 2016)
Los Angeles	2014.11-2016.03	MWO [c]	80	20	(Miller et al., 2020)
Beijing	2014	WLG [d]	75.2 ± 14.6	24.8	(Niu et al., 2016)
Xiamen	2014	WLG	59.1 ± 26.8	40.9	(Niu et al., 2016)
Xi'an	2014 winter	WLG	92.7 ± 9.7	7.3 ± 9.7	(Zhou et al., 2020)
Xi'an, urban	2016 summer	WLG	82.5 ± 23.8	17.5	(Wang et al., 2018)
Xi'an, urban	2016 winter	WLG	61.8 ± 10.6	38.2	(Wang et al., 2018)
Xi'an, suburban	2016 summer	WLG	90.0 ± 24.8	10.0	(Wang et al., 2018)
Xi'an, suburban	2016 winter	WLG	57.4 ± 9.7	42.6	(Wang et al., 2018)
Guangzhou	2022 winter	NL [e]	79 ± 5	21	this study
Shenzhen	2022 winter	NL	73 ± 6	27	this study
Zhanjiang	2022 winter	NL	59 ± 4	41	this study
Shaoguan	2022 winter	NL	53 ± 13	47	this study

[a] Mace Head, [b] La Jolla, [c] Mount Wilson Observatory, [d] Waliguan, [e] Nanling

https://doi.org/10.5194/egusphere-2025-1931
Preprint. Discussion started: 25 June 2025

Table E2 Comparison of C_{ff} concentrations derived from $\Delta(^{14}CO_2)$ measurements in various cities

Country	City	Time	C_{ff} (μmol mol^{-1})	References
Poland	Krakow	1989	27.5	(Kuc et al., 2003)
Poland	Krakow	1994	10	(Kuc et al., 2003)
Poland	Krakow	2005−2009	1.98−2.18	(Zimnoch et al., 2012)
Poland	Kasprowy Wierch	2005−2009	1.95−2.08	(Zimnoch et al., 2012)
Poland	Gliwice	2011.01−2013.01	23−24	(Piotrowska et al., 2020)
Czech Republic	Prague	2001−2018	25.51 ± 11.45	(Svetlik et al., 2010)
Slovakia	Bratislava	1999−2007	25.56 ± 6.90	(Svetlik et al., 2010)
Germany	Heidelberg	1986−1996	11.09 ± 0.24	(Levin and Rödenbeck, 2008)
Germany	Heidelberg	1997−2007	10.92 ± 0.34	(Levin and Rödenbeck, 2008)
Hungary	Debrecen	2009/10.01	10−15	(Molnár et al., 2010)
France	Paris	2010.01−02	26.4	(Lopez et al., 2013)
United Kingdom	London	2020.06−07	17.3 ± 3.0	(Zazzeri et al., 2023)
United States	Los Angeles	2006−2013	22.9 ± 5.6	(Newman et al., 2016)
United States	Los Angeles	2014.11−2016.03	13.2 ± 9.4	(Miller et al., 2020)
United States	Indianapolis	2010−2015	10.8 ± 1.0	(Turnbull et al., 2015)
China	Urumqi	2014−2016	45.6 ± 12.9	(Zhou et al., 2020)
China	Lanzhou	2014−2016	36.4 ± 8.8	(Zhou et al., 2020)
China	Xi'an	2011−2013	40.1 ± 3.8	(Zhou et al., 2022)
China	Xi'an	2014−2016	25.7 ± 1.1	(Zhou et al., 2022)
China	Suburban Xi'an	2016	23.5 ± 6.5	(Wang et al., 2018)
China	Near Xi'an	2021.04−2022.03	13.1 ± 10.9	(Liu et al., 2024)
China	Beijing	2014	39.7 ± 36.1	(Niu et al., 2016)
China	Beijing	2014−2016	27.0 ± 0.3	(Zhou et al., 2020)
China	Beijing	2020 winter	19.7 ± 22.0	(Wang et al., 2022b)
China	Wuhan	2014−2016	34.5 ± 10.0	(Zhou et al., 2020)
China	Xiamen	2014	13.6 ± 12.3	(Niu et al., 2016)
China	Guangzhou	2011	23.7 ± 12.9	(Ding et al., 2013)

https://doi.org/10.5194/egusphere-2025-1931
Preprint. Discussion started: 25 June 2025

China	Guangzhou	2022	15.3 ± 5.2	this study
China	Shenzhen	2022	13.7 ± 10.2	this study
China	Zhanjiang	2022	10.0 ± 5.2	this study
China	Shaoguan	2022	8.2 ± 7.0	this study

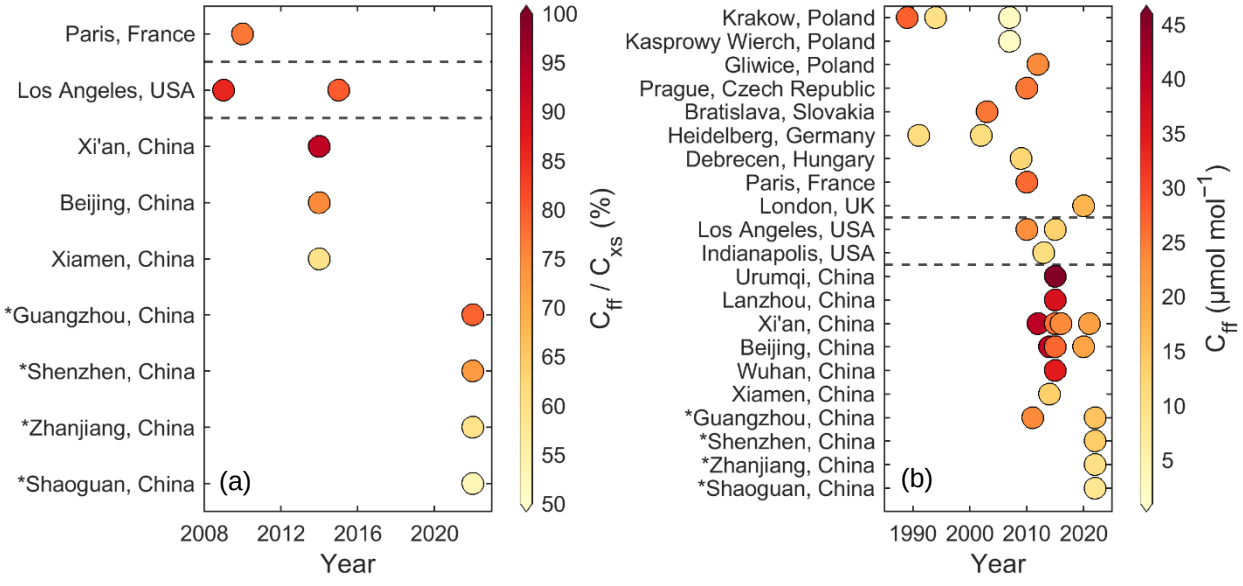

Figure E1 Comparison of **(a)** C_{ff} fractions in C_{xs} and **(b)** C_{ff} concentrations derived from $\Delta(^{14}CO_2)$ measurements from previous studies and this study (*) in various cities across European countries (Kuc et al., 2003; Levin and Rödenbeck, 2008; Molnár et al., 2010; Svetlik et al., 2010; Zimnoch et al., 2012; Lopez et al., 2013; Piotrowska et al., 2020; Zazzeri et al., 2023), United States (Turnbull et al., 2015; Newman et al., 2016; Miller et al., 2020), and China (Ding et al., 2013; Niu et al., 2016; Zhou et al., 2020; Wang et al., 2022b; Liu et al., 2024; Zhou et al., 2022). In (a), Los Angeles, Beijing, Guangzhou, and Shenzhen are megacities, Xi'an is a supercity, and other are large and medium cities (Council, 2022). Values in (a) and (b) refer to Tables E1 and E2, respectively.

https://doi.org/10.5194/egusphere-2025-1931
Preprint. Discussion started: 25 June 2025

Appendix F: HYSPLIT back trajectories and FLEXPART footprints

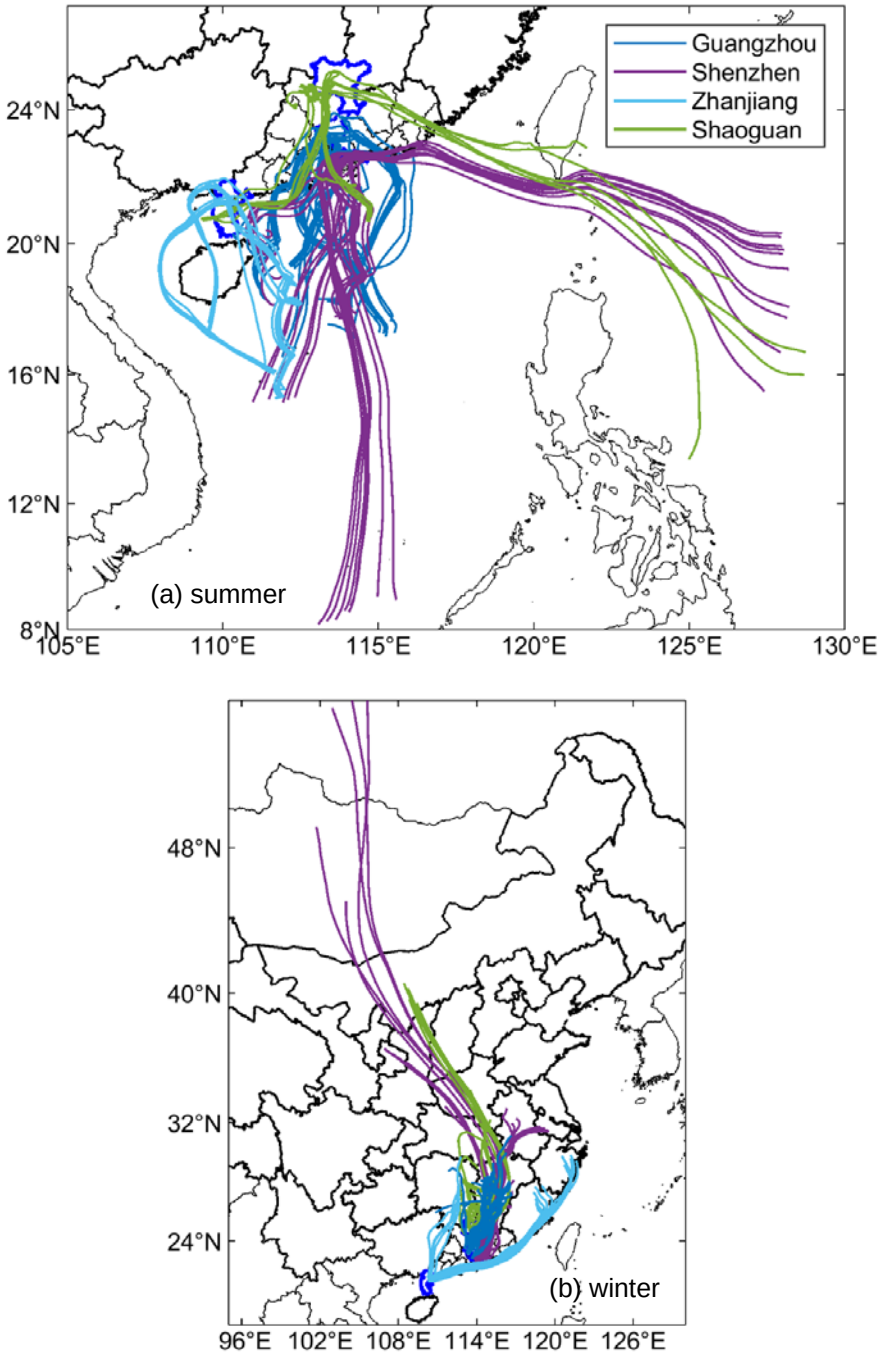

https://doi.org/10.5194/egusphere-2025-1931
Preprint. Discussion started: 25 June 2025

Figure F1 HYSPLIT back trajectories for a 72-h duration for Guangzhou, Shenzhen, Zhanjiang, and Shaoguan in **(a)** summer and **(b)** winter. National boundaries were taken from Natural Earth (https://www.naturalearthdata.com/, last accessed: 9 March 2024).

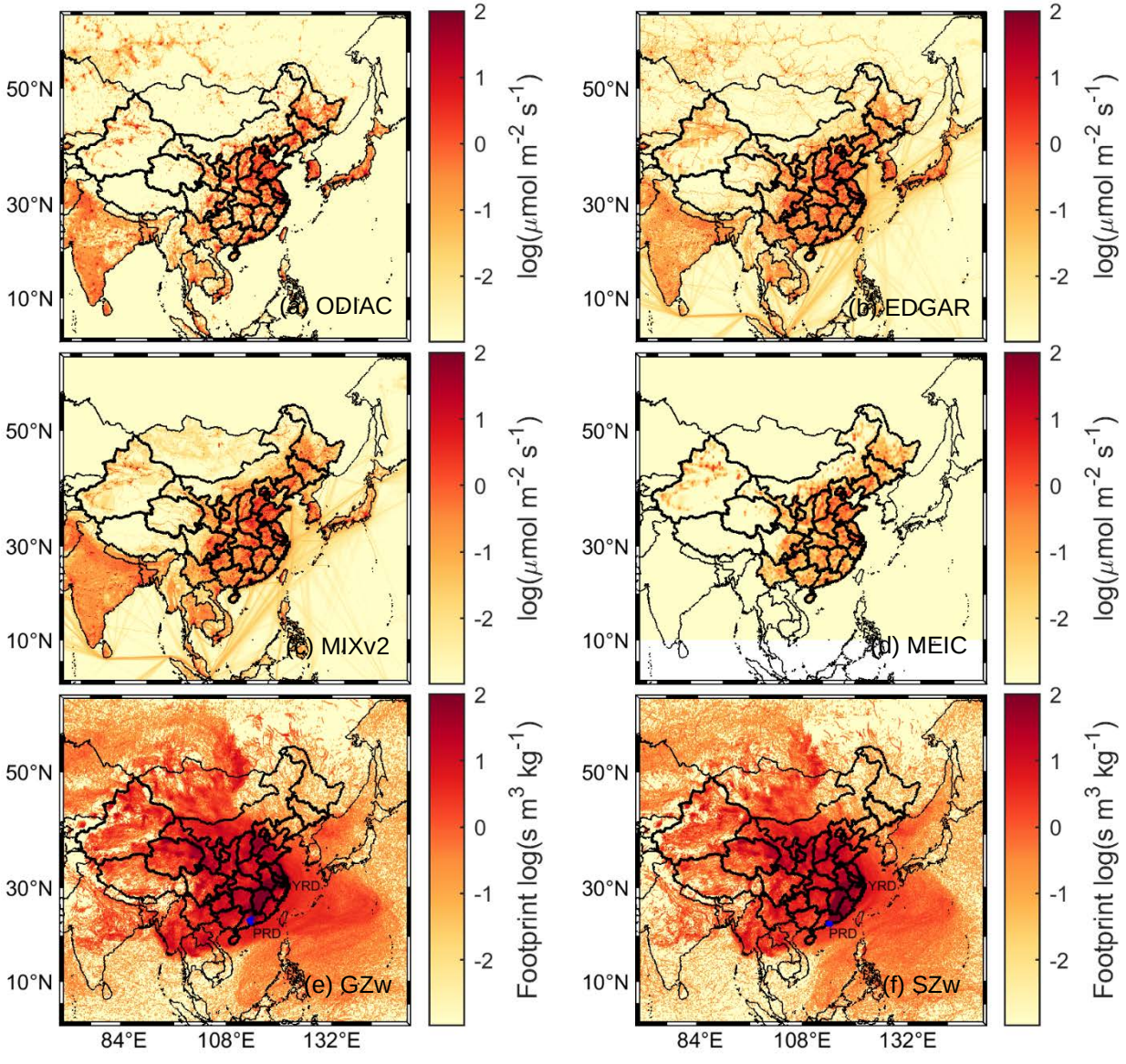

Figure F2 Annual mean C_{ff} emissions in China from four gridded inventory datasets: **(a)** ODIAC, **(b)** EDGAR, **(c)** MIXv2, and **(d)** MEIC, and FLEXPART footprints simulating C_{ff} emissions for **(e)** Guangzhou (GZ), **(f)** Shenzhen (SZ) in winter (w) by releasing particles at the blue sampling sites at heights from 0–100 m a.s.l. over a period of 30 days. The YRD and PRD

https://doi.org/10.5194/egusphere-2025-1931
Preprint. Discussion started: 25 June 2025

represent Yangtze River Delta and Pearl River Delta urban agglomeration labelled in (e) and (f). Boundaries of nations and Chinese provinces were obtained from Natural Earth (https://www.naturalearthdata.com/, last accessed: 9 March 2024).

Appendix G: Comparison of contributions of coal, oil and natural gas to C_{ff} concentrations in various cities

Table G1 Comparison of contributions of coal, oil and natural gas to C_{ff} concentrations in various cities

City	Time	F_{coal} (%)	F_{oil} (%)	F_{ng} (%)	References
Paris	2010	< 1	30	70	(Lopez et al., 2013)
Los Angeles	2007.10	< 1	69	31	(Djuricin et al., 2010)
Los Angeles	2007.12	< 1	61	39	(Djuricin et al., 2010)
Los Angeles	2008.02	< 1	58	42	(Djuricin et al., 2010)
Los Angeles	2008.04	< 1	52	48	(Djuricin et al., 2010)
Los Angeles	2006-2013 winter	< 1	68	32	(Newman et al., 2016)
Los Angeles	2006-2013 summer	< 1	55	45	(Newman et al., 2016)
Xi'an	2014 winter	72.6 ± 10.4	13.8 ± 10.4	13.6	(Zhou et al., 2014)
Xi'an	2019.12-2020.01	54 ± 4	24 ± 14	22 ± 13	(Wang et al., 2022b)
Beijing	2020.12-2021.01	17 ± 10	28 ± 19	55 ± 9	(Wang et al., 2022b)
Guangzhou	2022 winter	49 ± 25	29 ± 22	22 ± 19	this study
Shenzhen	2022 winter	47 ± 25	29 ± 21	24 ± 20	this study
Zhanjiang	2022 winter	43 ± 24	29 ± 21	28 ± 21	this study
Shaoguan	2022 winter	39 ± 24	34 ± 23	27 ± 21	this study

https://doi.org/10.5194/egusphere-2025-1931
Preprint. Discussion started: 25 June 2025

Appendix H: $R_{CO/CO2ff}$ for sites, cities and comparison

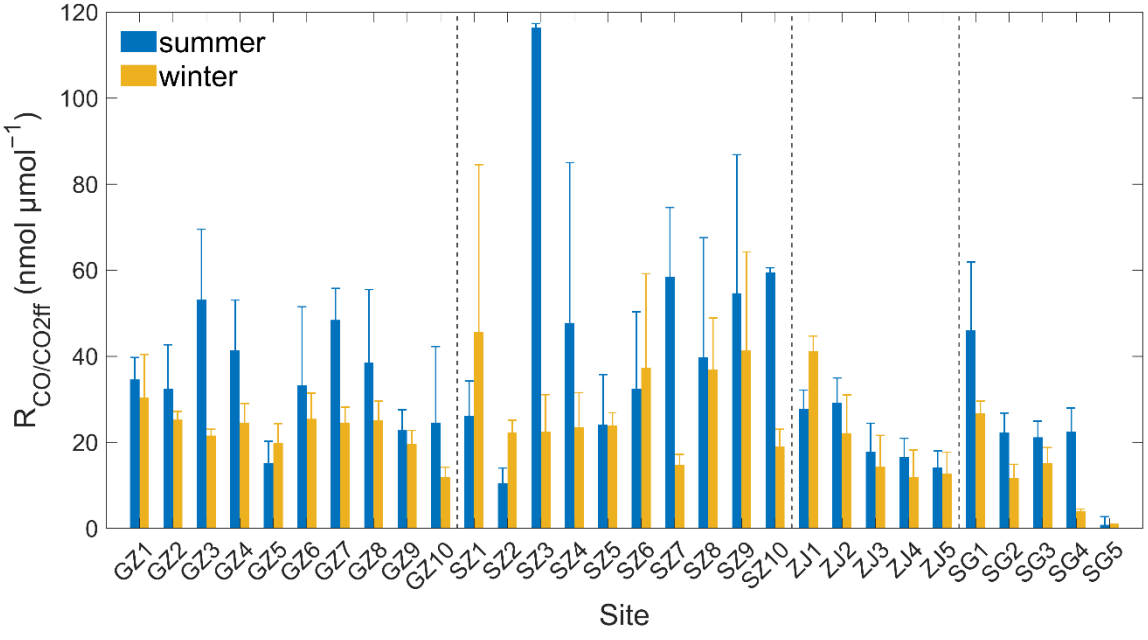

Figure H1 $R_{CO/CO2ff}$ averages at the 30 sampling sites

695

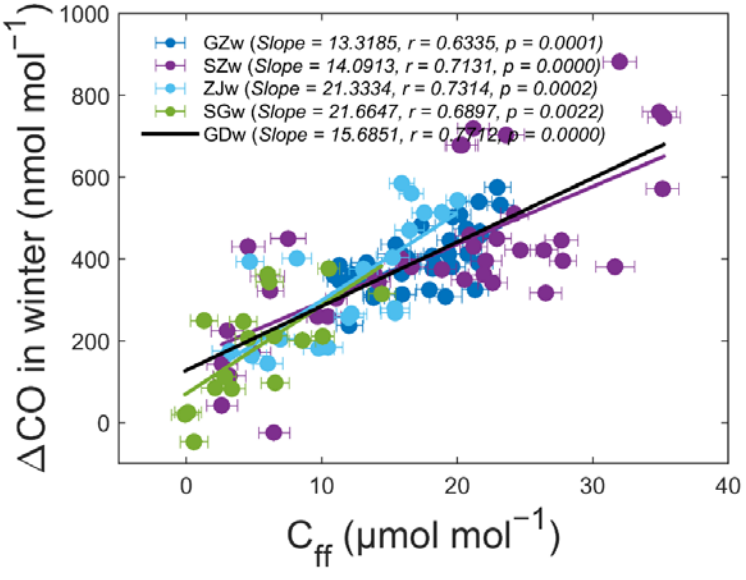

Figure H2 ΔCO: C_{ff} for Guangzhou, Shenzhen, Zhanjiang, and Shaoguan in winter

https://doi.org/10.5194/egusphere-2025-1931
Preprint. Discussion started: 25 June 2025

Table H1 Observational emission ratios of CO to C_{ff} ($R_{CO/CO2ff}$) for China and Chinese cities

City	Time	$R_{CO/CO2ff}$ (nmol μmol^{-1})	Method [a]	References
China	2001	68.8	I	(Suntharalingam et al., 2004)
China	2004−2010	44 ± 3	II	(Turnbull et al., 2011)
China	1998	56.3	I	(Tohjima et al., 2014)
China	2010	37.5	I	(Tohjima et al., 2014)
Mainland China	2009	36.3	I	(Fu et al., 2015)
Yellow Sea	2016	35.0	I	(Tang et al., 2018)
China, CN [b]	2014−2016	31 ± 8	II	(Lee et al., 2020)
China, CE [b]	2014−2016	36 ± 2	II	(Lee et al., 2020)
China, CB [b]	2014−2016	29 ± 8	II	(Lee et al., 2020)
China, OB [b]	2014−2016	31 ± 4	II	(Lee et al., 2020)
Beijing	2005	54.3	I	(Han et al., 2009)
Beijing/Tianjin	2009−2010	59.5	I	(Silva et al., 2013)
Beijing	2014	30.4 ± 1.6	II	(Niu et al., 2018)
Rural Beijing	2004	72.3	I	(Wang et al., 2010)
Rural Beijing	2005	52.5	I	(Wang et al., 2010)
Rural Beijing	2006	48.1	I	(Wang et al., 2010)
Rural Beijing	2007	43.7	I	(Wang et al., 2010)
Rural Beijing	2008	47.0	I	(Wang et al., 2010)
Rural Beijing	2009−2010	47 ± 2	II	(Turnbull et al., 2011)
Xi'an	2016	46 ± 13	II	(Wang et al., 2018)
Near Xi'an	2021	23 ± 6	II	(Liu et al., 2024)
Xiamen	2014	29.6 ± 3	II	(Niu et al., 2018)
Guangzhou	2009−2010	35.8	I	(Silva et al., 2013)
Guangzhou	2014−2017 winter	23.8	I	(Mai et al., 2021)
Guangzhou	2022 winter	13.3 ± 0.00002	II	Fig. H2, this study
Shenzhen	2022 winter	14.1 ± 0.000003	II	Fig. H2, this study
Zhanjiang	2022 winter	21.3 ± 0.00002	II	Fig. H2, this study

https://doi.org/10.5194/egusphere-2025-1931
Preprint. Discussion started: 25 June 2025

Shaoguan	2022 winter	21.7 ± 0.00004	II	Fig. H2, this study

[a] by correction from $R_{CO/CO2}$ by increased 20 % (Method I) and estimation from $\Delta^{14}C$ measurements (Method II), [b] CN represents the air masses from northeast China, CE for central eastern China around the Shandong area, CB for continental background air, and OB for ocean background.

Code availability

The FLEXPART 10.4 model is available at https://www.flexpart.eu/. The MixSIAR 3.1.12 model is available via GitHub at https://brianstock.github.io/MixSIAR/index.html. The HYSPLIT model is available at https://www.arl.noaa.gov/hysplit/. In this study, commercial software such as MATLAB R2023a, and public software such as R 4.3.2 and Python 3.9 are used for data processing and result visualization.

Data availability

Data generated in this study are available in Supplement Dataset 1 and seasonal averages in Table A1. Additional data related to this paper may be requested from the corresponding authors. The Carnegie Ames Stanford Approach Global Fire Emissions Database Version 4 (CASA-GFED4s) dataset is available at https://daac.ornl.gov/VEGETATION/guides/fire_emissions_v4_R1.html. The CASA-GFED3 dataset is available at http://nacp-files.nacarbon.org/nacp-kawa-01/. The Open-source Data Inventory for Anthropogenic CO_2 (ODIAC) is available from https://db.cger.nies.go.jp/dataset/ODIAC/. The Emissions Database for Global Atmospheric Research (EDGAR) Global Greenhouse Gas and Air Pollutant Emissions are from https://edgar.jrc.ec.europa.eu. The Multi-resolution Emission Inventory for China (MEIC) and the Open Biomass Burning Emission Inventory for China (OBBEIC) are available from http://meicmodel.org.cn. The MIXv2 Asian emission inventory (MIXv2) is available from https://csl.noaa.gov/groups/csl4/modeldata/data/Li2023/. The National Centers for Environmental Prediction's Climate Forecast System (CFSv2) Reanalysis data that drive the FLEXPART model is available at https://rda.ucar.edu/datasets/ds094.0/. The National Centers for Environmental Prediction's Global Data Assimilation System (GDAS) Reanalysis data that drives the HYSPLIT model is available at ftp.arl.noaa.gov/pub/archives/reanalysis.

Author contribution

G.Z., D.C., Jun Li, and P.L. conceived and designed the study. Almost all authors participated in the sampling organized by Jun Li and P.L.. Z.N. provided data in Beijing and Xi'an. P.D. provided data from Ding et al., (2013) in Guangzhou. R.L. conducted the sample graphitization. Sanyuan Z. handled the ^{14}C measurement by AMS. P.L. and B.L. performed the

https://doi.org/10.5194/egusphere-2025-1931
Preprint. Discussion started: 25 June 2025

simulations. P.L. conducted the data search and analysis, and wrote the article, with contributions from G.Z., Jun Li, Z.C., Jing L., and T.Z. for revisions and improvements.

Competing interests

The authors declare no competing interest.

Acknowledgements

We gratefully acknowledge the research team from Professor Gan Zhang's group for their essential support in air sampling, including staff scientists, postdoctoral researchers, and graduate students. Special thanks are extended to Mr. Jiangtao Li for his dedicated assistance with field sampling and laboratory extraction procedures.

Financial support

This study was supported by the National Natural Science Foundation of China (NSFC; nos. 42330715, 42103082, 42030715, and 42177241), Guangdong Provincial Applied Science and Technology Research and Development Program (Grant nos. 2022A1515011271, and 2022A1515011851), the Alliance of International Science Organizations (Grant no. ANSO-CR-KP-2021-05), China Postdoctoral Science Foundation (Grant no. 2022T150652), Special Research Assistant Program of the Chinese Academy of Sciences (CAS), and Director's Fund of Guangzhou Institute of Geochemistry, CAS (Grant no. 2021SZJJ-3).

References

Akagi, S. K., Yokelson, R. J., Wiedinmyer, C., Alvarado, M. J., Reid, J. S., Karl, T., Crounse, J. D., and Wennberg, P. O.: Emission factors for open and domestic biomass burning for use in atmospheric models, Atmos. Chem. Phys., 11, 4039-4072, 10.5194/acp-11-4039-2011, 2011.

Bakwin, P. S., Tans, P. P., White, J. W. C., and Andres, R. J.: Determination of the isotopic($^{13}C/^{12}C$) discrimination by terrestrial biology from a global network of observations, Global Biogeochem. Cy., 12, 555–562, https://doi.org/10.1029/98GB02265, 1998.

Chen, Y., Yao, B., Wu, J., Yang, H., Ding, A., Liu, S., Li, X., O'Doherty, S., Li, J., Li, Y., Yu, H., Wang, W., Chen, L., Yang, X., Fu, T.-M., Shen, H., Ye, J., Wang, C., and Zhu, L.: Observations and emission constraints of trichlorofluoromethane (CFC-11) in southeastern China: first-year results from a new AGAGE station, Environ. Res. Lett., 19, 074043, 10.1088/1748-9326/ad5857, 2024.

Cheng, P., Xiao, X. M., Tian, H., Huang, B. J., Wilkins, R. W. T., and Zhang, Y. Z.: Source controls on geochemical characteristics of crude oils from the Qionghai Uplift in the western Pearl River Mouth Basin, offshore South China Sea, Mar. Pet. Geol., 40, 85–98, https://doi.org/10.1016/j.marpetgeo.2012.10.003, 2013.

Coplen, T. B.: New guidelines for reporting stable hydrogen, carbon, and oxygen isotope-ratio data, Geochim. Cosmochim. Ac., 60, 3359–3360, 1996.

https://doi.org/10.5194/egusphere-2025-1931
Preprint. Discussion started: 25 June 2025

Council, O. o. t. L. G. f. t. S. N. P. C. o. t. S., Guo, D., and She, J. (Eds.): Tabulation on 2020 China Population Census by County, China Statistics Press, Beijing, China2022.

Crippa, M., Guizzardi, D., Pagani, F., Banja, M., Muntean, M., E., S., Becker, W., Monforti-Ferrario, F., Quadrelli, R., Risquez Martin, A., Taghavi-Moharamli, P., Köykkä, J., Grassi, G., Rossi, S., Brandao De Melo, J., Oom, D., Branco, A., San-Miguel, J., and Vignati, E.: GHG emissions of all world countries, Publications Office of the European Union, LuxembourgJRC134504, 10.2760/953322, 2023.

Dhakal, S.: Urban energy use and carbon emissions from cities in China and policy implications, Energy Policy, 37, 4208–4219, https://doi.org/10.1016/j.enpol.2009.05.020, 2009.

Ding, P., Shen, C., Yi, W., Wang, N., Ding, X., Fu, D., and Liu, K.: Fossil-Fuel-Derived CO_2 Contribution to the Urban Atmosphere in Guangzhou, South China, Estimated by $^{14}CO_2$ Observation, 2010–2011, Radiocarbon, 55, 791–803, 2013.

Djuricin, S., Pataki, D. E., and Xu, X.: A comparison of tracer methods for quantifying CO_2 sources in an urban region, J. Geophys. Res. Atmos., 115, D11303, https://doi.org/10.1029/2009JD012236, 2010.

Duren, R. M. and Miller, C. E.: Measuring the carbon emissions of megacities, Nature Clim. Change, 2, 560–562, 10.1038/nclimate1629, 2012.

Emissions Database for Global Atmospheric Research (EDGAR_2024_GHG): https://edgar.jrc.ec.europa.eu/dataset_ghg2024, last

ICOS ATC CO_2 Release, Jungfraujoch (13.9 m), 2016-12-12–2024-03-31, ICOS RI: https://hdl.handle.net/11676/4-Kot58QX1b5u-e8SGD8XTPy (last accessed: 28 July 2024) last

ICOS ATC/CAL ^{14}C Release, Jungfraujoch (6.0 m), 2015-09-21–2023-10-02, ICOS RI: https://hdl.handle.net/11676/6c_RZ7NHc2dnZv7d84BMY_YY (last accessed: 28 July 2024) last

Friedlingstein, P., O'Sullivan, M., Jones, M. W., Andrew, R. M., Bakker, D. C. E., Hauck, J., Landschützer, P., Le Quéré, C., Luijkx, I. T., Peters, G. P., Peters, W., Pongratz, J., Schwingshackl, C., Sitch, S., Canadell, J. G., Ciais, P., Jackson, R. B., Alin, S. R., Anthoni, P., Barbero, L., Bates, N. R., Becker, M., Bellouin, N., Decharme, B., Bopp, L., Brasika, I. B. M., Cadule, P., Chamberlain, M. A., Chandra, N., Chau, T. T. T., Chevallier, F., Chini, L. P., Cronin, M., Dou, X., Enyo, K., Evans, W., Falk, S., Feely, R. A., Feng, L., Ford, D. J., Gasser, T., Ghattas, J., Gkritzalis, T., Grassi, G., Gregor, L., Gruber, N., Gürses, Ö., Harris, I., Hefner, M., Heinke, J., Houghton, R. A., Hurtt, G. C., Iida, Y., Ilyina, T., Jacobson, A. R., Jain, A., Jarníková, T., Jersild, A., Jiang, F., Jin, Z., Joos, F., Kato, E., Keeling, R. F., Kennedy, D., Klein Goldewijk, K., Knauer, J., Korsbakken, J. I., Körtzinger, A., Lan, X., Lefèvre, N., Li, H., Liu, J., Liu, Z., Ma, L., Marland, G., Mayot, N., McGuire, P. C., McKinley, G. A., Meyer, G., Morgan, E. J., Munro, D. R., Nakaoka, S. I., Niwa, Y., O'Brien, K. M., Olsen, A., Omar, A. M., Ono, T., Paulsen, M., Pierrot, D., Pocock, K., Poulter, B., Powis, C. M., Rehder, G., Resplandy, L., Robertson, E., Rödenbeck, C., Rosan, T. M., Schwinger, J., Séférian, R., Smallman, T. L., Smith, S. M., Sospedra-Alfonso, R., Sun, Q., Sutton, A. J., Sweeney, C., Takao, S., Tans, P. P., Tian, H., Tilbrook, B., Tsujino, H., Tubiello, F., van der Werf, G. R., van Ooijen, E., Wanninkhof, R., Watanabe, M., Wimart-Rousseau, C., Yang, D., Yang, X., Yuan, W., Yue, X., Zaehle, S., Zeng, J., and Zheng, B.: Global Carbon Budget 2023, Earth Syst. Sci. Data, 15, 5301-5369, 10.5194/essd-15-5301-2023, 2023a.

Friedlingstein, P., O'Sullivan, M., Jones, M. W., Andrew, R. M., Bakker, D. C. E., Hauck, J., Landschützer, P., Le Quéré, C., Luijkx, I. T., Peters, G. P., Peters, W., Pongratz, J., Schwingshackl, C., Sitch, S., Canadell, J. G., Ciais, P., Jackson, R. B., Alin, S. R., Anthoni, P., Barbero, L., Bates, N. R., Becker, M., Bellouin, N., Decharme, B., Bopp, L., Brasika, I. B. M., Cadule, P., Chamberlain, M. A., Chandra, N., Chau, T. T. T., Chevallier, F., Chini, L. P., Cronin, M., Dou, X., Enyo, K., Evans, W., Falk, S., Feely, R. A., Feng, L., Ford, D. J., Gasser, T., Ghattas, J., Gkritzalis, T., Grassi, G., Gregor, L., Gruber, N., Gürses, Ö., Harris, I., Hefner, M., Heinke, J., Houghton, R. A., Hurtt, G. C., Iida, Y., Ilyina, T., Jacobson, A. R., Jain, A., Jarníková, T., Jersild, A., Jiang, F., Jin, Z., Joos, F., Kato, E., Keeling, R. F., Kennedy, D., Klein Goldewijk, K., Knauer, J., Korsbakken, J. I., Körtzinger, A., Lan, X., Lefèvre, N., Li, H., Liu, J., Liu, Z., Ma, L., Marland, G., Mayot, N., McGuire, P. C., McKinley, G. A., Meyer, G., Morgan, E. J., Munro, D. R., Nakaoka, S. I., Niwa, Y., O'Brien, K. M., Olsen, A., Omar, A. M., Ono, T., Paulsen, M., Pierrot, D., Pocock, K., Poulter, B., Powis, C. M., Rehder, G., Resplandy, L., Robertson, E., Rödenbeck, C., Rosan, T. M., Schwinger, J., Séférian, R., Smallman, T. L., Smith, S. M., Sospedra-Alfonso, R., Sun, Q., Sutton, A. J., Sweeney, C., Takao, S., Tans, P. P., Tian, H., Tilbrook, B., Tsujino, H., Tubiello, F., van der Werf, G. R., van Ooijen, E., Wanninkhof, R., Watanabe, M., Wimart-Rousseau, C., Yang, D., Yang, X., Yuan, W., Yue, X., Zaehle, S., Zeng, J., and Zheng, B.: Global Carbon Budget 2023, Earth Syst. Sci. Data, 15, 5301–5369, 10.5194/essd-15-5301-2023, 2023b.

https://doi.org/10.5194/egusphere-2025-1931
Preprint. Discussion started: 25 June 2025

Fu, X., Zhang, H., Lin, C.-J., Feng, X., Zhou, L., and Fang, S.: Correlation slopes of GEM/CO, GEM/CO_2, and GEM/CH_4 and estimated mercury emissions in China, South Asia, the Indochinese Peninsula, and Central Asia derived from observations in northwestern and southwestern China, Atmos. Chem. Phys., 15, 1013–1028, 2015.

Graven, H., Fischer, M. L., Lueker, T., Jeong, S., Guilderson, T. P., Keeling, R. F., Bambha, R., Brophy, K., Callahan, W., Cui, X., Frankenberg, C., Gurney, K. R., LaFranchi, B. W., Lehman, S. J., Michelsen, H., Miller, J. B., Newman, S., Paplawsky, W., Parazoo, N. C., Sloop, C., and Walker, S. J.: Assessing fossil fuel CO_2 emissions in California using atmospheric observations and models, Environ. Res. Lett., 13, 065007, 10.1088/1748-9326/aabd43, 2018.

Graven, H. D. and Gruber, N.: Continental-scale enrichment of atmospheric 14CO2 from the nuclear power industry: Potential impact on the estimation of fossil fuel-derived CO2, Atmos. Chem. Phys., 11, 12339-12349, 2011.

Graven, H. D., Stephens, B. B., Guilderson, T. P., Campos, T. L., Schimel, D. S., Campbell, J. E., and Keeling, R. F.: Vertical profiles of biospheric and fossil fuel-derived CO_2 and fossil fuel CO_2:CO ratios from airborne measurements of $\Delta^{14}C$, CO_2 and CO above Colorado, USA, Tellus B, 61, 536-546, https://doi.org/10.1111/j.1600-0889.2009.00421.x, 2009.

Gurney, K. R., Liang, J. M., Roest, G., Song, Y., Mueller, K., and Lauvaux, T.: Under-reporting of greenhouse gas emissions in U.S. cities, Nat. Commun., 12, 553, 10.1038/s41467-020-20871-0, 2021.

Han, P., Zeng, N., Oda, T., Lin, X., Crippa, M., Guan, D., Janssens-Maenhout, G., Ma, X., Liu, Z., and Shan, Y.: Evaluating China's fossil-fuel CO_2 emissions from a comprehensive dataset of nine inventories, Atmos. Chem. Phys., 20, 11371–11385, 2020.

Han, S., Kondo, Y., Oshima, N., Takegawa, N., Miyazaki, Y., Hu, M., Lin, P., Deng, Z., Zhao, Y., and Sugimoto, N.: Temporal variations of elemental carbon in Beijing, J. Geophys. Res. Atmos., 114, D23202, 2009.

Hua, Q., Turnbull, J. C., Santos, G. M., Rakowski, A. Z., Ancapichún, S., De Pol-Holz, R., Hammer, S., Lehman, S. J., Levin, I., and Miller, J. B.: Atmospheric radiocarbon for the period 1950–2019, Radiocarbon, 1-23, 2021.

Huang, X., Li, M., Li, J., and Song, Y.: A high-resolution emission inventory of crop burning in fields in China based on MODIS Thermal Anomalies/Fire products, Atmos. Environ., 50, 9-15, https://doi.org/10.1016/j.atmosenv.2012.01.017, 2012.

IAEA: Management of waste containing tritium and carbon-14, Technical Report Series No. 421, International Atomic Energy Agency, Vienna, Austria2004.

Karion, A., Lopez-Coto, I., Gourdji, S. M., Mueller, K., Ghosh, S., Callahan, W., Stock, M., DiGangi, E., Prinzivalli, S., and Whetstone, J.: Background conditions for an urban greenhouse gas network in the Washington, DC, and Baltimore metropolitan region, Atmos. Chem. Phys., 21, 6257–6273, 10.5194/acp-21-6257-2021, 2021.

Kuc, T., Rozanski, K., Zimnoch, M., Necki, J. M., and Korus, A.: Anthropogenic emissions of CO_2 and CH_4 in an urban environment, Appl. Energy, 75, 193–203, https://doi.org/10.1016/S0306-2619(03)00032-1, 2003.

Atmospheric Carbon Dioxide Dry Air Mole Fractions from the NOAA GML Carbon Cycle Cooperative Global Air Sampling Network, 1968-2022, Version: 2023-08-28: https://doi.org/10.15138/wkgj-f215, last

Le Quéré, C., Andrew, R. M., Canadell, J. G., Sitch, S., Korsbakken, J. I., Peters, G. P., Manning, A. C., Boden, T. A., Tans, P. P., Houghton, R. A., Keeling, R. F., Alin, S., Andrews, O. D., Anthoni, P., Barbero, L., Bopp, L., Chevallier, F., Chini, L. P., Ciais, P., Currie, K., Delire, C., Doney, S. C., Friedlingstein, P., Gkritzalis, T., Harris, I., Hauck, J., Haverd, V., Hoppema, M., Klein Goldewijk, K., Jain, A. K., Kato, E., Körtzinger, A., Landschützer, P., Lefèvre, N., Lenton, A., Lienert, S., Lombardozzi, D., Melton, J. R., Metzl, N., Millero, F., Monteiro, P. M. S., Munro, D. R., Nabel, J. E. M. S., Nakaoka, S., O'Brien, K., Olsen, A., Omar, A. M., Ono, T., Pierrot, D., Poulter, B., Rödenbeck, C., Salisbury, J., Schuster, U., Schwinger, J., Séférian, R., Skjelvan, I., Stocker, B. D., Sutton, A. J., Takahashi, T., Tian, H., Tilbrook, B., van der Laan-Luijkx, I. T., van der Werf, G. R., Viovy, N., Walker, A. P., Wiltshire, A. J., and Zaehle, S.: Global Carbon Budget 2016, Earth Syst. Sci. Data, 8, 605-649, 10.5194/essd-8-605-2016, 2016.

Lee, H., Dlugokencky, E. J., Turnbull, J. C., Lee, S., Lehman, S. J., Miller, J. B., Pétron, G., Lim, J. S., Lee, G. W., Lee, S. S., and Park, Y. S.: Observations of atmospheric $^{14}CO_2$ at Anmyeondo GAW station, South Korea: implications for fossil fuel CO_2 and emission ratios, Atmos. Chem. Phys., 20, 12033–12045, 10.5194/acp-20-12033-2020, 2020.

Levin, I. and Rödenbeck, C.: Can the envisaged reductions of fossil fuel CO_2 emissions be detected by atmospheric observations?, Naturwissenschaften, 95, 203–208, 2008.

Levin, I., Kromer, B., Schmidt, M., and Sartorius, H.: A novel approach for independent budgeting of fossil fuel CO_2 over Europe by $^{14}CO_2$ observations, Geophys. Res. Lett., 30, 2194, 2003.

https://doi.org/10.5194/egusphere-2025-1931
Preprint. Discussion started: 25 June 2025

Lewis, C. W., Klouda, G. A., and Ellenson, W. D.: Radiocarbon measurement of the biogenic contribution to summertime PM-2.5 ambient aerosol in Nashville, TN, Atmos. Environ., 38, 6053-6061, https://doi.org/10.1016/j.atmosenv.2004.06.011, 2004.

Li, L.: A Decade of Transformative Achievements in Energy Consumption Revolution (in Chinese), 2023.

Li, M., Liu, H., Geng, G., Hong, C., Liu, F., Song, Y., Tong, D., Zheng, B., Cui, H., Man, H., Zhang, Q., and He, K.: Anthropogenic emission inventories in China: a review, Natl. Sci. Rev., 4, 834–866, 10.1093/nsr/nwx150 %J National Science Review, 2017.

Li, M., Kurokawa, J., Zhang, Q., Woo, J. H., Morikawa, T., Chatani, S., Lu, Z., Song, Y., Geng, G., Hu, H., Kim, J., Cooper, O. R., and McDonald, B. C.: MIXv2: a long-term mosaic emission inventory for Asia (2010–2017), Atmos. Chem. Phys., 24, 3925–3952, 10.5194/acp-24-3925-2024, 2024.

Li, M., Zhang, Q., Zheng, B., Tong, D., Lei, Y., Liu, F., Hong, C., Kang, S., Yan, L., Zhang, Y., Bo, Y., Su, H., Cheng, Y., and He, K.: Persistent growth of anthropogenic non-methane volatile organic compound (NMVOC) emissions in China during 1990–2017: drivers, speciation and ozone formation potential, Atmos. Chem. Phys., 19, 8897–8913, 10.5194/acp-19-8897-2019, 2019.

Liu, W., Niu, Z., Feng, X., Zhou, W., Liang, D., Lyu, M., Wang, G., Lu, X., Liu, L., and Turnbull, J. C.: Atmospheric CO_2 and $^{14}CO_2$ observations at the northern foot of the Qinling Mountains in China: Temporal characteristics and source quantification, Sci. Total Environ., 920, 170682, https://doi.org/10.1016/j.scitotenv.2024.170682, 2024.

Lo Vullo, E. and Monforti, F.: Fossil CO_2 and GHG emissions of all world countries, 10.2760/687800, 2019.

Lopez, M., Schmidt, M., Delmotte, M., Colomb, A., Gros, V., Janssen, C., Lehman, S. J., Mondelain, D., Perrussel, O., Ramonet, M., Xueref-Remy, I., and Bousquet, P.: CO, NO_x and $^{13}CO_2$ as tracers for fossil fuel CO_2: results from a pilot study in Paris during winter 2010, Atmos. Chem. Phys., 13, 7343–7358, 10.5194/acp-13-7343-2013, 2013.

Mai, B., Deng, X., Liu, X., Li, T., Guo, J., and Ma, Q.: The climatology of ambient CO_2 concentrations from long-term observation in the Pearl River Delta region of China: Roles of anthropogenic and biogenic processes, Atmos. Environ., 251, 118266, https://doi.org/10.1016/j.atmosenv.2021.118266, 2021.

(Ministry of Ecology and Environment of China), China Ecological Environment Statistical Annual Report in 2019 (in Chinese): https://www.mee.gov.cn/hjzl/sthjzk/sthjtjnb/202108/W020210827611248993188.pdf (last accessed: 14 March 2025) last

Multi-resolution Emission Inventory model for China: http://meicmodel.org.cn (last accessed: 14 March 2024) last

Miller, J. B. and Tans, P. P.: Calculating isotopic fractionation from atmospheric measurements at various scales, Tellus B, 55, 207–214, https://doi.org/10.1034/j.1600-0889.2003.00020.x, 2003.

Miller, J. B., Lehman, S. J., Verhulst, K. R., Miller, C. E., Duren, R. M., Yadav, V., Newman, S., and Sloop, C. D.: Large and seasonally varying biospheric CO_2 fluxes in the Los Angeles megacity revealed by atmospheric radiocarbon, Proc. Natl. Acad. Sci., 117, 26681–26687, 2020.

Mohn, J., Szidat, S., Fellner, J., Rechberger, H., Quartier, R., Buchmann, B., and Emmenegger, L.: Determination of biogenic and fossil CO2 emitted by waste incineration based on 14CO2 and mass balances, Bioresour. Technol., 99, 6471-6479, https://doi.org/10.1016/j.biortech.2007.11.042, 2008.

Molnár, M., Major, I., Haszpra, L., Světlík, I., Svingor, É., and Veres, M.: Fossil fuel CO_2 estimation by atmospheric ^{14}C measurement and CO_2 mixing ratios in the city of Debrecen, Hungary, J. Radioanal. Nucl., 286, 471–476, 10.1007/s10967-010-0791-2, 2010.

Newman, S., Xu, X., Gurney, K. R., Hsu, Y. K., Li, K. F., Jiang, X., Keeling, R., Feng, S., O'Keefe, D., Patarasuk, R., Wong, K. W., Rao, P., Fischer, M. L., and Yung, Y. L.: Toward consistency between trends in bottom-up CO_2 emissions and top-down atmospheric measurements in the Los Angeles megacity, Atmos. Chem. Phys., 16, 3843–3863, 10.5194/acp-16-3843-2016, 2016.

Niu, Z., Zhou, W., Huang, Y., Wang, S., Zhang, G., Feng, X., Lu, X., Lyu, M., and Turnbull, J. C.: Identification of Urban Carbon Emission Peaks through Tree-Ring 14C, Environ. Sci. Technol., 58, 17313-17319, 10.1021/acs.est.4c06041, 2024.

Niu, Z., Zhou, W., Feng, X., Feng, T., Wu, S., Cheng, P., Lu, X., Du, H., Xiong, X., and Fu, Y.: Atmospheric fossil fuel CO_2 traced by $^{14}CO_2$ and air quality index pollutant observations in Beijing and Xiamen, China, Environ. Sci. Pollut. R., 25, 17109–17117, 10.1007/s11356-018-1616-z, 2018.

https://doi.org/10.5194/egusphere-2025-1931
Preprint. Discussion started: 25 June 2025

Niu, Z. C., Zhou, W. J., Wu, S. G., Cheng, P., Lu, X., Xiong, X., Du, H., Fu, Y., and Wang, G.: Atmospheric fossil fuel CO_2 traced by $\Delta^{14}C$ in Beijing and Xiamen, China: temporal variations, inland/coastal differences and influencing factors, Environ. Sci. Technol., 50, 5474–5480, 2016.

Oda, T. and Maksyutov, S.: A very high-resolution (1 km×1 km) global fossil fuel CO_2 emission inventory derived using a point source database and satellite observations of nighttime lights, Atmos. Chem. Phys., 11, 543–556, 10.5194/acp-11-543-2011, 2011.

ODIAC Fossil Fuel CO_2 Emissions Dataset (Version name: ODIAC2022), Center for Global Environmental Research, National Institute for Environmental Studies. (Reference date: 2024/01/22): https://db.cger.nies.go.jp/dataset/ODIAC/, last

Pataki, D. E., Ehleringer, J. R., Flanagan, L. B., Yakir, D., Bowling, D. R., Still, C. J., Buchmann, N., Kaplan, J. O., and Berry, J. A.: The application and interpretation of Keeling plots in terrestrial carbon cycle research, Global Biogeochem. Cy., 17, 1022, https://doi.org/10.1029/2001GB001850, 2003.

Ping, H., Chen, H., Zhu, J., George, S. C., Mi, L., Pang, X., and Zhai, P.: Origin, source, mixing, and thermal maturity of natural gases in the Panyu lower uplift and the Baiyun depression, Pearl River Mouth Basin, northern South China Sea, AAPG Bull., 102, 2171–2200, 10.1306/04121817160 %J AAPG Bulletin, 2018.

Piotrowska, N., Pazdur, A., Pawełczyk, S., Rakowski, A. Z., Sensuła, B., and Tudyka, K.: Human Activity Recorded in Carbon Isotopic Composition of Atmospheric CO_2 in Gliwice Urban Area and Surroundings (Southern Poland) in the Years 2011–2013, Radiocarbon, 62, 141–156, 10.1017/RDC.2019.92, 2020.

Pisso, I., Sollum, E., Grythe, H., Kristiansen, N. I., Cassiani, M., Eckhardt, S., Arnold, D., Morton, D., Thompson, R. L., Groot Zwaaftink, C. D., Evangeliou, N., Sodemann, H., Haimberger, L., Henne, S., Brunner, D., Burkhart, J. F., Fouilloux, A., Brioude, J., Philipp, A., Seibert, P., and Stohl, A.: The Lagrangian particle dispersion model FLEXPART version 10.4, Geosci. Model Dev., 12, 4955–4997, 10.5194/gmd-12-4955-2019, 2019.

Quan, Y., Liu, J., Hao, F., Bao, X., Xu, S., Teng, C., and Wang, Z.: Geochemical characteristics and origins of natural gas in the Zhu III sub-basin, Pearl River Mouth Basin, China, Mar. Pet. Geol., 101, 117–131, 10.1016/j.marpetgeo.2018.12.007, 2018.

Global Fire Emissions Database, Version 4.1 (GFEDv4): https://doi.org/10.3334/ORNLDAAC/1293, last

Rosendahl, C.: Proxy to fossil-fuel CO2 emission ratios: in-situ versus inventory data, 2022.

Saha, S., Moorthi, S., Wu, X., Wang, J., Nadiga, S., Tripp, P., Behringer, D., Hou, Y.-T., Chuang, H.-y., Iredell, M., Ek, M., Meng, J., Yang, R., Mendez, M. P., van den Dool, H., Zhang, Q., Wang, W., Chen, M., and Becker, E.: NCEP Climate Forecast System Version 2 (CFSv2) Selected Hourly Time-Series Products, Research Data Archive at the National Center for Atmospheric Research, Computational and Information Systems Laboratory [dataset], 2011.

Shi, Q., Zheng, B., Zheng, Y., Tong, D., Liu, Y., Ma, H., Hong, C., Geng, G., Guan, D., He, K., and Zhang, Q.: Co-benefits of CO_2 emission reduction from China's clean air actions between 2013-2020, Nat. Commun., 13, 5061, 10.1038/s41467-022-32656-8, 2022.

Silva, S. J., Arellano, A. F., and Worden, H. M.: Toward anthropogenic combustion emission constraints from space-based analysis of urban CO_2/CO sensitivity, Geophys. Res. Lett., 40, 4971–4976, https://doi.org/10.1002/grl.50954, 2013.

Song, Y., Liu, B., Miao, W., Chang, D., and Zhang, Y.: Spatiotemporal variation in nonagricultural open fire emissions in China from 2000 to 2007, Global Biogeochem. Cy., 23, https://doi.org/10.1029/2008GB003344, 2009.

Stein, A. F., Draxler, R. R., Rolph, G. D., Stunder, B. J. B., Cohen, M. D., and Ngan, F.: NOAA's HYSPLIT Atmospheric Transport and Dispersion Modeling System, Bulletin of the American Meteorological Society, 96, 2059–2077, 10.1175/bams-d-14-00110.1, 2015.

Stock, B., Jackson, A., Ward, E., Parnell, A., Phillips, D., and Semmens, B.: Analyzing mixing systems using a new generation of Bayesian tracer mixing models, PeerJ, 10.7287/peerj.preprints.26884, 2018.

Stuiver, M. and Polach, H. A.: Discussion reporting of ^{14}C data, Radiocarbon, 19, 355–363, 1977.

Suntharalingam, P., Jacob, D. J., Palmer, P. I., Logan, J. A., Yantosca, R. M., Xiao, Y., Evans, M. J., Streets, D. G., Vay, S. L., and Sachse, G. W.: Improved quantification of Chinese carbon fluxes using CO_2/CO correlations in Asian outflow, J. Geophys. Res. Atmos., 109, D18S18, https://doi.org/10.1029/2003JD004362, 2004.

Svetlik, I., Povinec, P. P., Molnár, M., Vána, M., Šivo, A., and Bujtás, T.: Radiocarbon in the Air of Central Europe: Long-Term Investigations, Radiocarbon, 52, 823–834, 10.1017/S0033822200045847, 2010.

Tang, W., Arellano, A. F., DiGangi, J. P., Choi, Y., Diskin, G. S., Agustí-Panareda, A., Parrington, M., Massart, S., Gaubert, B., Lee, Y., Kim, D., Jung, J., Hong, J., Hong, J. W., Kanaya, Y., Lee, M., Stauffer, R. M., Thompson, A. M., Flynn, J. H.,

https://doi.org/10.5194/egusphere-2025-1931
Preprint. Discussion started: 25 June 2025

and Woo, J. H.: Evaluating high-resolution forecasts of atmospheric CO and CO_2 from a global prediction system during KORUS-AQ field campaign, Atmos. Chem. Phys., 18, 11007–11030, 10.5194/acp-18-11007-2018, 2018.

Tanimoto, H., Sawa, Y., Yonemura, S., Yumimoto, K., Matsueda, H., Uno, I., Hayasaka, T., Mukai, H., Tohjima, Y., Tsuboi, K., and Zhang, L.: Diagnosing recent CO emissions and ozone evolution in East Asia using coordinated surface observations, adjoint inverse modeling, and MOPITT satellite data, Atmos. Chem. Phys., 8, 3867–3880, 10.5194/acp-8-3867-2008, 2008.

Tohjima, Y., Kubo, M., Minejima, C., Mukai, H., Tanimoto, H., Ganshin, A., Maksyutov, S., Katsumata, K., Machida, T., and Kita, K.: Temporal changes in the emissions of CH_4 and CO from China estimated from CH_4/CO_2 and CO/CO_2 correlations observed at Hateruma Island, Atmos. Chem. Phys., 14, 1663–1677, 2014.

Turnbull, J., Rayner, P., Miller, J., Naegler, T., Ciais, P., and Cozic, A.: On the use of $^{14}CO_2$ as a tracer for fossil fuel CO_2: Quantifying uncertainties using an atmospheric transport model, J. Geophys. Res. Atmos., 114, D22302, 2009.

Turnbull, J. C., Miller, J., Lehman, S., Tans, P., Sparks, R., and Southon, J.: Comparison of $^{14}CO_2$, CO, and SF_6 as tracers for recently added fossil fuel CO_2 in the atmosphere and implications for biological CO_2 exchange, Geophys. Res. Lett., 33, L01817, 2006.

Turnbull, J. C., Tans, P. P., Lehman, S. J., Baker, D., Conway, T. J., Chung, Y. S., Gregg, J., Miller, J. B., Southon, J. R., and Zhou, L.-X.: Atmospheric observations of carbon monoxide and fossil fuel CO_2 emissions from East Asia, J. Geophys. Res. Atmos., 116, D24306, https://doi.org/10.1029/2011JD016691, 2011.

Turnbull, J. C., Sweeney, C., Karion, A., Newberger, T., Lehman, S. J., Tans, P. P., Davis, K. J., Lauvaux, T., Miles, N. L., Richardson, S. J., Cambaliza, M. O., Shepson, P. B., Gurney, K., Patarasuk, R., and Razlivanov, I.: Toward quantification and source sector identification of fossil fuel CO_2 emissions from an urban area: Results from the INFLUX experiment, J. Geophys. Res. Atmos., 120, 292–312, https://doi.org/10.1002/2014JD022555, 2015.

van der Werf, G. R., Randerson, J. T., Giglio, L., Collatz, G. J., Mu, M., Kasibhatla, P. S., Morton, D. C., DeFries, R. S., Jin, Y., and van Leeuwen, T. T.: Global fire emissions and the contribution of deforestation, savanna, forest, agricultural, and peat fires (1997–2009), Atmos. Chem. Phys., 10, 11707-11735, 10.5194/acp-10-11707-2010, 2010.

van der Werf, G. R., Randerson, J. T., Giglio, L., van Leeuwen, T. T., Chen, Y., Rogers, B. M., Mu, M., van Marle, M. J. E., Morton, D. C., Collatz, G. J., Yokelson, R. J., and Kasibhatla, P. S.: Global fire emissions estimates during 1997–2016, Earth Syst. Sci. Data, 9, 697-720, 10.5194/essd-9-697-2017, 2017.

Wang, P., Zhou, W., Niu, Z., Cheng, P., Wu, S., Xiong, X., Lu, X., and Du, H.: Emission characteristics of atmospheric carbon dioxide in Xi'an, China based on the measurements of CO_2 concentration, $\Delta^{14}C$ and $\delta^{13}C$, Sci. Total Environ., 619, 1163–1169, 2018.

Wang, P., Zhou, W., Xiong, X., Wu, S., Niu, Z., Cheng, P., Du, H., and Hou, Y.: Stable carbon isotopic characteristics of fossil fuels in China, Sci. Total Environ., 805, 150240, https://doi.org/10.1016/j.scitotenv.2021.150240, 2022a.

Wang, P., Zhou, W., Xiong, X., Wu, S., Niu, Z., Yu, Y., Liu, J., Feng, T., Cheng, P., Du, H., Lu, X., Chen, N., and Hou, Y.: Source attribution of atmospheric CO_2 using ^{14}C and ^{13}C as tracers in two Chinese megacities during winter, J. Geophys. Res. Atmos., 127, e2022JD036504, https://doi.org/10.1029/2022JD036504, 2022b.

Wang, Y., Munger, J., Xu, S., McElroy, M. B., Hao, J., Nielsen, C., and Ma, H.: CO_2 and its correlation with CO at a rural site near Beijing: implications for combustion efficiency in China, Atmos. Chem. Phys., 10, 8881–8897, 2010.

Wen, X. F., Meng, Y., Zhang, X. Y., Sun, X. M., and Lee, X.: Evaluating calibration strategies for isotope ratio infrared spectroscopy for atmospheric $^{13}CO_2/^{12}CO_2$ measurement, Atmos. Meas. Tech., 6, 1491–1501, 10.5194/amt-6-1491-2013, 2013.

Wu, F., Li, F., Zhao, X., Bolan, N. S., Fu, P., Lam, S. S., Mašek, O., Ong, H. C., Pan, B., Qiu, X., Rinklebe, J., Tsang, D. C. W., Van Zwieten, L., Vithanage, M., Wang, S., Xing, B., Zhang, G., and Wang, H.: Meet the challenges in the "Carbon Age", Carbon Research, 1, 1, 10.1007/s44246-022-00001-9, 2022.

Xu, R., Tong, D., Xiao, Q., Qin, X., Chen, C., Yan, L., Cheng, J., Cui, C., Hu, H., Liu, W., Yan, X., Wang, H., Liu, X., Geng, G., Lei, Y., Guan, D., He, K., and Zhang, Q.: MEIC-global-CO_2: A new global CO_2 emission inventory with highly-resolved source category and sub-country information, Sci. China Earth Sci., 67, 450–465, 10.1007/s11430-023-1230-3, 2024.

Xu, X., Trumbore, S. E., Zheng, S., Southon, J. R., McDuffee, K. E., Luttgen, M., and Liu, J. C.: Modifying a sealed tube zinc reduction method for preparation of AMS graphite targets: Reducing background and attaining high precision, Nuclear Instruments and Methods in Physics Research Section B: Beam Interactions with Materials and Atoms, 259, 320–329, https://doi.org/10.1016/j.nimb.2007.01.175, 2007.

https://doi.org/10.5194/egusphere-2025-1931
Preprint. Discussion started: 25 June 2025

Nuclear Power Industry Report: The Development of Fourth-Generation Nuclear Power Accelerates, and Controllable Nuclear Fusion Moves Forward Steadily (in Chinese): https://pdf.dfcfw.com/pdf/H3_AP202401221617892738_1.pdf?1705938486000.pdf (last accessed: 14 March 2025) last

Zazzeri, G., Graven, H., Xu, X., Saboya, E., Blyth, L., Manning, A., Chawner, H., Wu, D., and Hammer, S.: Radiocarbon Measurements Reveal Underestimated Fossil CH_4 and CO_2 Emissions in London, Geophys. Res. Lett., 50, e2023GL103834, 10.1029/2023GL103834, 2023.

Zhang, L., Ruan, J., Zhang, Z., Qin, Z., Lei, Z., Cai, B., Wang, S., and Tang, L.: City-level pathways to carbon peak and neutrality in China, Cell Reports Sustainability, 1, 100102, https://doi.org/10.1016/j.crsus.2024.100102, 2024.

Zhang, Q., Zheng, Y., Tong, D., Shao, M., Wang, S., Zhang, Y., Xu, X., Wang, J., He, H., Liu, W., Ding, Y., Lei, Y., Li, J., Wang, Z., Zhang, X., Wang, Y., Cheng, J., Liu, Y., Shi, Q., Yan, L., Geng, G., Hong, C., Li, M., Liu, F., Zheng, B., Cao, J., Ding, A., Gao, J., Fu, Q., Huo, J., Liu, B., Liu, Z., Yang, F., He, K., and Hao, J.: Drivers of improved $PM_{2.5}$ air quality in China from 2013 to 2017, Proc. Natl. Acad. Sci., 116, 24463–24469, doi:10.1073/pnas.1907956116, 2019.

Zheng, B., Tong, D., Li, M., Liu, F., Hong, C., Geng, G., Li, H., Li, X., Peng, L., Qi, J., Yan, L., Zhang, Y., Zhao, H., Zheng, Y., He, K., and Zhang, Q.: Trends in China's anthropogenic emissions since 2010 as the consequence of clean air actions, Atmos. Chem. Phys., 18, 14095–14111, 10.5194/acp-18-14095-2018, 2018.

Zheng, Y., Cao, W., Zhao, H., Chen, C., Lei, Y., Feng, Y., Qi, Z., Wang, Y., Wang, X., Xue, W., and Yan, G.: Identifying Key Sources for Air Pollution and CO2 Emission Co-control in China, Environ. Sci. Technol., 10.1021/acs.est.4c03299, 2024.

Zhou, W., Wu, S., Huo, W., Xiong, X., Cheng, P., Lu, X., and Niu, Z.: Tracing fossil fuel CO_2 using $\Delta^{14}C$ in Xi'an City, China, Atmos. Environ., 94, 538–545, 2014.

Zhou, W., Niu, Z., Wu, S., Xiaohu, X., Wang, P., Cheng, P., Hou, Y., du, H., Chen, N., and Lu, X.: Recent progress in atmospheric fossil fuel CO_2 trends traced by radiocarbon in China, Radiocarbon, 64, 1–11, 10.1017/RDC.2022.32, 2022.

Zhou, W. J., Niu, Z. C., Wu, S. G., Xiong, X., Hou, Y., Wang, P., Feng, T., Cheng, P., Du, H., and Lu, X.: Fossil fuel CO_2 traced by radiocarbon in fifteen Chinese cities, Sci. Total Environ., 729, 138639, 2020.

Zhou, Z., Li, P., Cheng, Z., Li, J., Li, J., Chen, D., Zhang, T., Xiong, X., Sa, R., Ma, S., and Zhang, G.: Selection of background stations and values for urban atmospheric $\Delta^{14}CO_2$ observation: a case study in Shenzhen (in Chinese), Geochimica, 53, 309–319, 2024.

Zhu, S., Ding, P., Wang, N., Shen, C., Jia, G., and Zhang, G.: The compact AMS facility at Guangzhou Institute of Geochemistry, Chinese Academy of Sciences, Nuclear Instruments and Methods in Physics Research Section B: Beam Interactions with Materials and Atoms, 361, 72–75, 2015.

Zimnoch, M., Jelen, D., Galkowski, M., Kuc, T., Necki, J., Chmura, L., Gorczyca, Z., Jasek, A., and Rozanski, K.: Partitioning of atmospheric carbon dioxide over Central Europe: insights from combined measurements of CO_2 mixing ratios and their carbon isotope composition, Isot. Environ. Health Stud., 48, 421–433, 10.1080/10256016.2012.663368, 2012.